HIGH ANGULAR RESOLUTION MEASUREMENTS IN INFRARED ASTRONOMY

by

M. P. STOKELD

A Thesis submitted for the degree of Doctor of Philosophy of the University of London and for the Diploma of Imperial College.

Astronomy Group
Blackett Laboratory
Imperial College
London SW7

July 1981

CONTENTS

page

PREFACE

ACKNOWLEDGEMENTS

INTRODUCTION

Chapter 1. Speckle Interferometry 3

1.1 The Speckle phenomenon 3

1.1.1 The instantaneous atmosphere-telescope MTF 4
1.1.2 The long exposure MTF 5
1.1.3 The short exposure MTF 7

1.2 The Infrared seeing 11

1.2.1 Temporal coherence 11
1.2.2 Atmospheric dispersion 14
1.2.3 Exposure time 15

1.3 Speckle limiting magnitudes 17

1.3.1 The Slit method 17
1.3.2 The Grid method 20

1.4 Object intensity reconstruction 23

1.4.1 Binary star separations 23
1.4.2 Centrosymmetric objects 23
1.4.3 Direct Fourier deconvolution 24
1.4.4 Speckles as images 24
1.4.5 Phase of speckles 24
1.4.6 Active optics 24

Chapter 2. Techniques and Instrumentation 26

2.1 The Slit technique: image analysis 26

2.1.1 Signal processing 27
2.1.2 Data analysis 29

2.2 The Grid technique: image analysis 33

2.2.1 Signal processing and data analysis 34

		page
2.3	Observational technique	34
2.4	The Observational system	35
2.4.1	Analogue electronics	37
2.4.2	Digital electronics	39
Chapter 3.	Results	45
3.1	Introduction	45
3.2	Results	45
Chapter 4.	The Lunar Occultation technique	52
4.1	Historical Summary	52
4.2	The Occultation event	52
4.2.1	The reduction model	54
4.2.2	The stochastical method	56
4.2.3	Lunar Occultations disturbed by Scintillation	58
4.2.4	Electrical deconvolution	60
4.3	General Observational and Signal to Noise Considerations	61
Chapter 5.	Techniques and Instrumentation	65
5.1	The Observational method	65
5.2	Signal Processing and Data Acquisition	66
5.3	Occultation Reduction Files	66
Chapter 6.	Occultation Results	69
6.1	Computational tests and limiting resolution	69
6.2	The electrical system response	70
6.3	Measured stellar diameters	74
REFERENCES:	Speckle	84
	Occultation	85

Acknowledgements

Firstly I should like to thank Mike Selby for providing me with the opportunity of doing this research work.

Outstanding help from Alain Chelli and Steve Morris proved invaluable, and I am glad to acknowledge the help given by Victor and Mick in the electronics lab. Finally, thank you Yvonne for the typing.

Preface

This thesis contains a description of experimental work carried out at Imperial College betweeen January 1978 and April 1981. Two projects have been developed, Speckle Interferometry and the Lunar Occultation technique. A large proportion of the work concerned methods of reducing raw data.

In the introductory chapter, the theoretical description of the atmosphere is presented and the derivation of the short and long exposure MTFs is reviewed. The subsequent sections contain pertinent information for the Speckle technique at infrared wavelengths, a consideration of limiting magnitudes for the slit and grid methods and, finally, ways of reconstructing the object intensity distribution.

Chapter 2 describes image analysis, signal and data processing. The observational technique detector system, electronics and computer systems used for measurements are reported. Chapter 3 presents results for the two Speckle methods and indicates how the technique might be improved.

Chapter 4 gives a brief Historical review of angular diameter measurements from Lunar Occultations and is followed by a description of the classical and scintillation models used to fit the data. A method of deducing the limiting angular diameter is given.

The penultimate chapter describes the observational method relevant for the 1.5m flux collector at Tenerife. The data reduction computer files and their arrangement are presented.

Finally, chapter 6 reports tests on the classical model, and four angular diameter measurements using both models are reported.

Introduction

Spatial interferometry in infrared astronomy is in its infancy and is still a long way from fulfilling its full astronomical potential. The development of techniques and instrumentation to determine the distribution of intensity across objects strongly emitting at IR wavelengths is motivated by three areas of interest: the solar system, stars with circumstellar envelopes and extragalactic nuclei.

Within the solar system particular interest lies in observing planetary surfaces and satellites. Jupiter is a classical example. Its cold surface (140K) is accented by hot spots, where underlying regions of the atmosphere (300K) emit directly into space. The volcanic activity of Io, Jupiter's third largest satellite and the search for ice caps on the Galilean satellites are other observational possibilities.

To date, most effort has been applied to measuring bright infrared stars with circumstellar envelopes. These emit at temperatures in the range 300-600K. One important reason for refining interferometric techniques is to discover planetary formation around such stars. This would be evident from the spatial structure and development of the envelope.

Late type stars with circumstellar shells returning matter to the interstellar medium is another possible area of study.

Very little work has so far been carried out on the spatial structure of extragalactic nuclei. Although in a lot of cases only moderate resolution is required to resolve nuclei (e.g. the extent for M82 is 10"), improvements in sensitivity and resolution are necessary to resolve complex structure and greater numbers of embedded sources. Perhaps the most promising galactic nuclei to study belong to Seyfert galaxies. Seyferts emit strongly in the IR. The nature of their nuclei is somewhat uncertain and depends upon correctly interpreting velocity differences of $10^6 ms^{-1}$ in their spectra.

The first part of this thesis describes Speckle Interferometry and its application at near infrared wavelengths (1-5 microns). Spatial measurements at these wavelengths have several advantages over those in the visible, due to the diminished effects of atmospheric turbulence. With increasing wavelength, temporal and correlation scales are increased. This means that the atmosphere appears frozen over longer

time intervals and the phase of the electromagnetic field (EM) is predictable over larger areas. Also atmospheric dispersion is reduced to the extent that it can be ignored, allowing larger spectral bandwidths to be used.

In addition to measuring the spatial intensity distribution of objects, techniques can be applied to measure the apparent angular diameters of single stars. If the parallax of the star and the total integrated flux at the Earth are known, the stellar radius and effective temperature, T_{eff}, can be calculated. The latter is used to calibrate excitation and colour temperatures which are essential to compare theory and observation. An accuracy of 1% in T_{eff} is required. This allows useful application of measurements of oscillator strengths, determined for stellar spectroscopy. However no technique is so far capable of this accuracy.

Part two of this thesis is dedicated to the Lunar Occultation technique. It is the biggest source of cool star angular diameters. The technique is capable of measurements in the range 1.5 to 15m arcsec. It encompasses spectral types in the range GØ-M9 and has been applied in the visible and near infrared.

The most accurate determination of angular diameters and effective temperatures is claimed by the indirect Infrared Flux method (Blackwell (1977)). Based on the insensitivity of the source flux of the star to temperature at an infrared wavelength, it combines model stellar atmosphere and measured absolute fluxes at the Earth. Given a sufficiently accurate flux, the method claims an accuracy superior to that of the intensity interferometer. It is hoped that some of our own measurements will serve as a check for the method.

Chapter 1 Speckle Interferometry

1.1 The Speckle phenomenon

The theoretical Rayleigh resolution limit for large telescopes cannot be attained for long exposure astronomical images. Atmospheric turbulence causes the EM field to be degraded, so that only small coherent areas exist across the telescope aperture. Many areas or phase cells contribute to the image and they form a fast-moving, finely-structured pattern, first interpreted as a speckle pattern by Labeyrie (1970). The speckles themselves are of the same size as the Airey disc and so contain spatial frequency information to the diffraction limit of the telescope. Normal time averaging adds speckle patterns to a blurred seeing disc and so destroys the high spatial frequencies, reducing the resolution.

Fried (1966) simplifies the description of atmospheric perturbations by introducing the parameter r_o, the Fried parameter, which is the distance across a typical phase cell. The angular resolution is then given by

$$\alpha = \frac{1.27\lambda}{r_o}$$

in the presence of turbulence. This approximately equals the diffraction-limited resolution of a telescope of diameter r_o. r_o itself is a statistical quantity depending upon the propagation path length and the strength of the turbulence. It is of the order of a few centimetres in the visible and tens of centimetres in the near infrared. Therefore a significant resolution loss is imposed by the atmosphere for normal observing techniques.

Labeyrie suggests a method for preserving information to the cut-off frequency of the telescope. The method is to sum speckle image power transforms (or autocorrelations). Comparison with a point source star allows the angular extension of the source to be determined by fitting a simple model in the Fourier plane. Recovery of the absolute source intensity distribution is not possible, as the phases of the speckles are lost.

The modification of the technique for near infrared wavelengths is

restricted by no image forming devices existing beyond one micron. However various possibilities exist, e.g. spatial filtering and detector arrays. The latter method is extremely expensive and still in an early stage of development. The methods of spatial filtering currently used involve either a set of grids or a single slit, across which the stellar image is oscillated at constant speed. For the former, each grid selects a spatial frequency in the image, so measurements are made separately (Selby et al. 1979). The slit method allows determination of the full spectrum (Sibille et al. 1979).

The principal difficulty with the technique is to account for the effects of variations in the atmospheric seeing. Unstable seeing conditions have hindered the methods from producing many good results, but continued refinements should enable the problem to be solved. Repeats of observations are useful to establish consistent results and the methods favour several nearby calibration stars.

1.1.1 The instantaneous atmosphere-telescope M.T.F.

Fourier mathematics is used to describe image formation and atmospheric blurring. The instantaneous image intensity for incoherent monochromatic radiation is given by

$$I(\underline{\alpha}) = O(\underline{\alpha}) * S(\underline{\alpha}) \qquad 1.1$$

where: $O(\underline{\alpha})$ is the object intensity function

$S(\underline{\alpha})$ is the pointspread function of the atmosphere-telescope system

$*$ denotes convolution

Equ.1.1 only strictly holds for two objects lying in the same isoplanatic patch. In the Fourier plane

$$I(\underline{f}) = O(\underline{f}).S(\underline{f}) \qquad 1.2$$

where $I(\underline{f})$ and $O(\underline{f})$ are the two-dimensional complex Fourier transforms of $I(\underline{\alpha})$ and $O(\underline{\alpha})$. $S(\underline{f})$ is the optical transfer function, (OTF), whose modulus is the modulation transfer function (MTF) which is used as a measure of optical system performance.

$S(\underline{f})$ is calculated by considering the image of a monochromatic

point source formed by an optical system looking through a turbulent atmosphere (Hufnagel (1964)). If $\psi_o(\underline{x})$ is the (perturbed) complex amplitude as collected by the telescope aperture, the Huygen-Fresnel diffraction theory predicts the disturbance in direction $\hat{\underline{\alpha}}$ to be

$$U(\underline{\alpha}) = \text{constant} \int_{\text{pupil}} \psi_o(\underline{x}) \exp(-i2\pi\underline{\alpha}.\underline{x}/\lambda) d\underline{x} \qquad (1.3)$$

This may be rewritten as

$$U(\underline{\alpha}) = \text{const} \int_{-\infty}^{\infty} \psi(\underline{u}) P(u) \exp(-i2n\underline{\alpha}.\underline{u}) d\underline{u} \qquad (1.4)$$

where $\psi(\underline{u}) = \psi_o(\lambda\underline{u})$ and $\underline{u} = \underline{x}/\lambda$

Here
$$P(\underline{u}) = \begin{cases} 1 & |u| \leq D/2\lambda \\ 0 & |u| \geq D/2\lambda \end{cases}$$

D = telescope diameter

The intensity in direction $\hat{\underline{\alpha}}$ is then

$$S(\underline{\alpha}) = \lambda^2/A \quad |FT(\psi(\underline{u})P(\underline{u})|^2 \qquad (1.5)$$

(A = telescope aperture area).

$S(\alpha)$ is normalised to unity at the origin for $\psi(u)=1$. The Fourier transform of Equ.1.5 is

$$S(\underline{f}) = \frac{\lambda^2}{A} \int_{-\infty}^{\infty} \psi^*(\underline{u}) \psi(\underline{u}+\underline{f}) P(\underline{u}) P(\underline{u}+\underline{f}) d\underline{u} \qquad (1.6)$$

In the absence of turbulence, the telescope MTF is just

$$T(\underline{f}) = \lambda^2/A \int_{-\infty}^{\infty} P(\underline{u}) P(\underline{u}+\underline{f}) d\underline{u} \qquad (1.7)$$

1.1.2 The long exposure MTF

The MTF for seeing is given by the ensemble average of Equ.1.6

$$\langle S(\underline{f}) \rangle = \lambda^2/A \int_{-\infty}^{\infty} \langle \psi^*(\underline{u}) \psi(\underline{u}+\underline{f}) \rangle P(\underline{u}) P(\underline{u}+\underline{f}) d\underline{u} \qquad (1.8)$$

The integral is simplified by the assumption that $\psi(\underline{u})$ is locally stationary w.r.t. translations in $\underline{x}$. The average term can be written

$$B_{\psi}(\underline{f}) = \langle \psi^{*}(\underline{u})\psi(\underline{u}+\underline{f}) \rangle \tag{1.9}$$

This is the second order moment of the complex amplitude. Thus, the long exposure MTF is

$$\langle S(f) \rangle = B_{\psi}(\underline{f})T(\underline{f}) \tag{1.10}$$

It is the product of the telescope MTF and the long exposure transfer function of the atmosphere.

The form of the atmospheric transfer function

Temperature, pressure and humidity changes affect the refractive index of the air and hence the light propagating through the atmosphere. The changes are due to turbulent elements. In particular, elements comparable or smaller than the telescope aperture alter the structure of an astronomical image.

Tatarski (1961) introduces the idea of a structure function which can be applied to measure the magnitude of fluctuating quantities such as temperature or refractive index. For a random function, the structure function is defined as

$$D_{f}(\tau) = \langle (f(t+\tau)-f(t))^{2} \rangle \tag{1.11}$$

which increases as the correlation over τ decreases and describes fluctuations in f(t) for periods $t \leq \tau$.

The MTF for a long exposure image can be expressed in terms of the "Wave structure function", D(r)†. Fried (1966) indicates that D(r) is of of the form

$$D(r) = Ar^{5/3}$$

where A is a constant dependent on the propagation path length and the strength of the turbulence along the path. D(r) simplifies

$$D(r) = 6.88(r/r_{o})^{5/3} \tag{1.12}$$

† The plane containing r lies parallel to the $\underline{x}$ plane.

by the introduction of the Fried parameter

$$r_o = (6.88/A)^{3/5} = (0.42k^2 \sec z \int C_n^2(h)dh)^{-3/5} \qquad (1.13)$$

where $C_n^2(h)$ is a constant of the refractive index structure function and

$k = \frac{2\pi}{\lambda}$, z is the zenith angle and h the altitude.

Fried shows that the second order moment of the complex amplitude is related to the wave structure function by the relation

$$B_\psi(f) = \exp(-\tfrac{1}{2}D(f)) = \exp(-3.44(f/f_o)^{5/3}) \qquad (1.14)$$

where $f = r/\lambda$ and $f_o = r_o/\lambda$.

Therefore the long exposure MTF is

$$S(f) = \exp(-3.44(f/f_o)^{5/3})T(f) \qquad (1.15)$$

S(f) is negligible for spatial frequencies $f>f_o$ and so information beyond f_o is lost.

1.1.3 The short exposure MTF

The classical Speckle technique consists of evaluating the ensemble average of a set of short exposure image power spectra:

$$\langle |I(\underline{f})|^2 \rangle = |O(\underline{f})|^2 \langle |S(\underline{f})|^2 \rangle \qquad (1.16)$$

The problem is to evaluate the power spectrum of a point source, $\langle |S(\underline{f})|^2 \rangle$, the Speckle MTF. Substitution from Equ.1.6 yields

$$\langle |S(\underline{f})|^2 \rangle = \lambda^4/A^2 \ .$$

$$\iint \langle \psi^*(\underline{u})\psi(\underline{u}+\underline{f})\psi(\underline{u}^1)\psi^*(\underline{u}^1+\underline{f}) \rangle \ P(\underline{u})P(\underline{u}+\underline{f})P(\underline{u}^1)P(\underline{u}^1+\underline{f})\,d\underline{u}d\underline{u}^1 \qquad (1.17)$$

where the averaged quantity is the fourth order moment of the complex amplitude. The solution of Equ.1.17 depends on the statistical distribution assumed for $\psi(u)$.

(i) The Normal model

For turbulence distributed equally with altitude the complex amplitude has a Gaussian or Normal distribution. In this case the averaged term in Equ.1.17 may be rewritten

$$\langle\psi^*(\underline{u})\psi(\underline{u}+\underline{f})\rangle\langle\psi(\underline{u}^1)\psi^*(\underline{u}^1+\underline{f})\rangle + \langle\psi^*(\underline{u})\psi(\underline{u}^1)\rangle\langle\psi(\underline{u}+\underline{f})\psi^*(\underline{u}^1+\underline{f})\rangle$$

Referring to Equ.1.9

$$\langle\psi^*(\underline{u})\psi(\underline{u}+\underline{f})\psi(\underline{u}^1)\psi^*(\underline{u}^1+\underline{f})\rangle = B^2(\underline{f}) + B^2(\underline{u}^1-\underline{u}) \qquad (1.18)$$

The expression

$$B_\psi(f) = \langle\psi^*(u)\psi(u+f)\rangle = \exp\left(-3.44(f/f_o)^{5/3}\right)$$

is approximately zero for $f>>f_o$ and shows that $\psi(u)$ and $\psi(u+f)$ are decorrelated. Only $B^2(u^1-u)$ contributes at these frequencies. Equ.1.17 reduces to

$$\langle|S(\underline{f})|^2\rangle = \lambda^4/A^2\int B^2(\underline{u}^1-\underline{u})P(\underline{u})P(\underline{u}+\underline{f})P(\underline{u}^1)P(\underline{u}^1+\underline{f})d\underline{u}d\underline{u}^1 \qquad (1.19)$$

Making the substitution $\underline{u}^1-\underline{u}=\underline{f}^1$

$$\langle|S(\underline{f})|^2\rangle = \lambda^4/A^2\int_{-\infty}^{+\infty}P(\underline{u})P(\underline{u}+\underline{f})\int_{-\infty}^{+\infty}B^2(\underline{f}^1)P(\underline{u}+\underline{f}^1)P(\underline{u}+\underline{f}+\underline{f}^1)d\underline{u}d\underline{f}^1$$

For a large telescope, $D>r_o$ and for $f<f_c-f_o$ ($f_c=\frac{D}{\lambda}$) the pupil function product is practically constant over the region where $B^2(f^1)$ takes on significant values. The second integral is then

$$\int B^2(\underline{f}^1)d\underline{f}^1 \simeq \sigma ,$$

the area of coherence of the complex amplitude. It is calculated by substituting the expression for $B^2(f)$. The result is

$$\sigma = 0.342\ f_o^2 = 0.342\ r_o^2/\lambda^2$$

Hence in the range $f_o < f. < f_c-f_o$

$$\langle|S(\underline{f})|^2\rangle = \lambda^2/A\ .\ \sigma\ \lambda^2/A\int_{-\infty}^{+\infty}P(\underline{u})P(\underline{u}+\underline{f})d\underline{u} = 0.342\ r_o^2\,T(f)/A \simeq \frac{1}{N}T(\underline{f}) \qquad (1.20)$$

where N is the number of Speckles.

The full expression for Equ.1.17 from Equ.1.18, Equ.1.10 and Equ.1.20 may now be evaluated.

$$\langle|S(\underline{f})|^2\rangle = B^2(\underline{f})T^2(\underline{f}) + T(\underline{f})/N = |\langle S(\underline{f})\rangle|^2 + T(\underline{f})/N. \qquad (1.21)$$

Equ.1.21 reveals that the Speckle MTF has two components (see Fig.1.1). The first is the long exposure MTF squared which contains no information on scales near the telescope limit. The second is the MTF of the telescope reduced by a factor dependent on the number of Speckles across the image. Equ.1.21 is valid provided the telescope is of sufficient quality to resolve the atmospherically induced seeing disc.

(ii) The Log-normal model

For turbulent layers restricted to the lower atmosphere, the statistical distribution of the complex amplitude is described by the Log-normal model. Both phase and log amplitude are described by zero mean Gaussian random functions, i.e. the modulus of the wave function is a constant. The fourth order moment of the wave function cannot be approximated by an analytical function. However, for low spatial frequencies the MTF is approximately

$$\langle|S(\underline{f})|^2\rangle_{\substack{SE \\ f\leq f_o}} \simeq T^2(\underline{f})\exp\left(-6.88(f/f_o)^{5/3}(1-(f/f_c)^{1/3})\right) \qquad (1.22)$$

Comparison with Equ.1.15 reveals an extra term in the exponent, which has the effect of reducing the seeing disc width. Furthermore, the short exposure MTF is not unique but is dependent upon the form of the aperture used. This can be understood from the following argument. Atmospherically induced corrugations of a stellar wavefront may be considered to be divided into those with scales larger and those smaller than the telescope pupil. The larger are seen by the telescope as wavefront tilts and their effect is to displace the image of the star in the focal plane. Smaller corrugations cause image blur. Therefore the size of the aperture and atmospheric correlation scale determine the nature of the short exposure seeing.

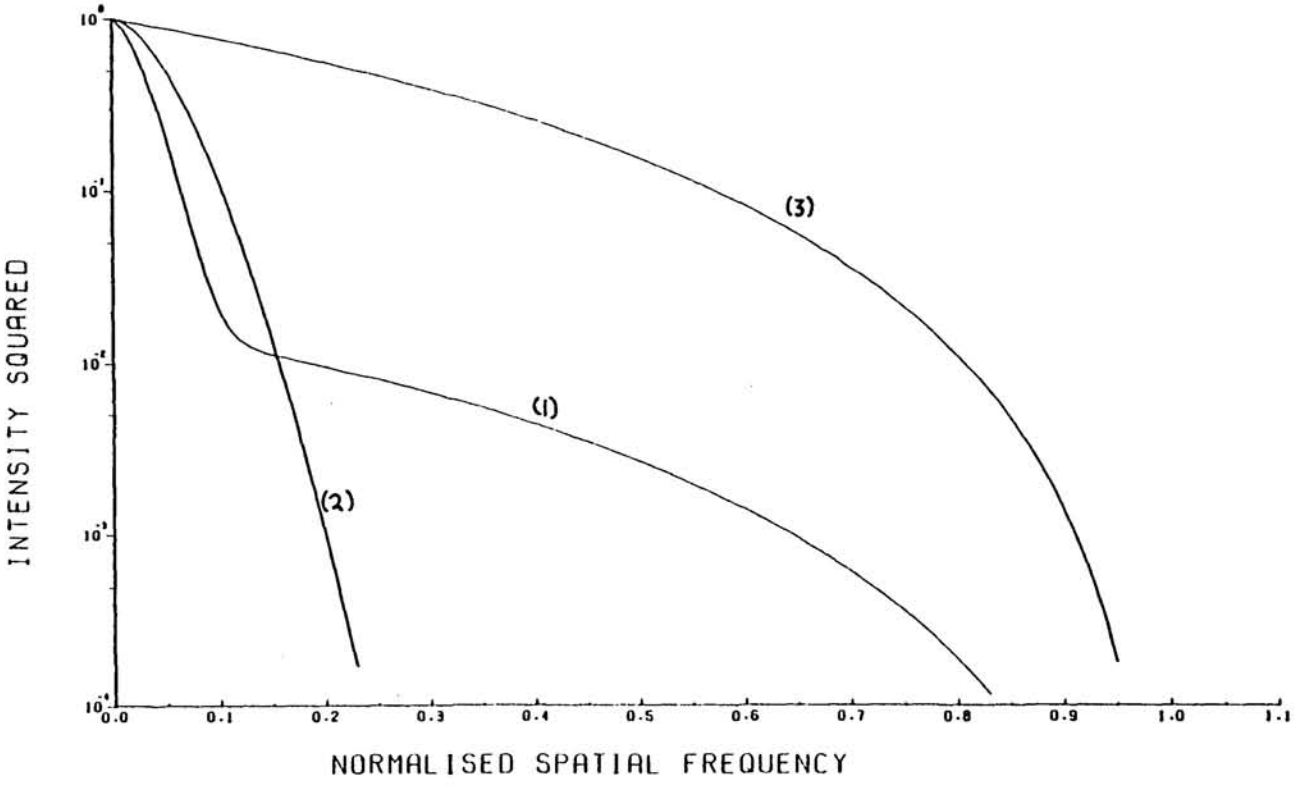


Fig.1.1 The Speckle MTF[1], atmospheric long exposure MTF squared[2] and the telescope MTF squared[3].

1.2 The Infrared seeing

The angular seeing disc in seconds of arc is of the order

$$\Delta\theta_s \simeq \frac{(1.27)206265\lambda}{r_o} \tag{1.23}$$

The Fried parameter, r_o, is itself a function of wavelength λ and zenith angle z, as indicated in Equ.1.13. More explicitly

$$r_o(\lambda) = r_o(\lambda_o)\left(\frac{\lambda}{\lambda_o}\right)^{1.2} (\cos z)^{0.6} \tag{1.24}$$

The IR seeing may then be estimated, given the visible seeing size

$$\Delta\theta_{s_1} = \Delta\theta_{s_2} \left(\frac{\lambda_2}{\lambda_1}\right)^{0.2} \tag{1.25}$$

Fig.1.2 plots the functional relationships depicted by Equs.1.24 and 1.25.

The ratio of Speckle MTF's with different seeing must not be confused with a possible source extension. Four such ratios are plotted in Fig.1.3 using the Normal model estimation of $<|S(f)|^2>$. The figure shows the ratioing method to be quite sensitive to variations in the Fried parameter and to have a characteristic form.

1.2.1 Temporal coherence

The visibility of IR Speckles is maintained by ensuring the maximum path difference across the image is less than the coherence length of the light, i.e.

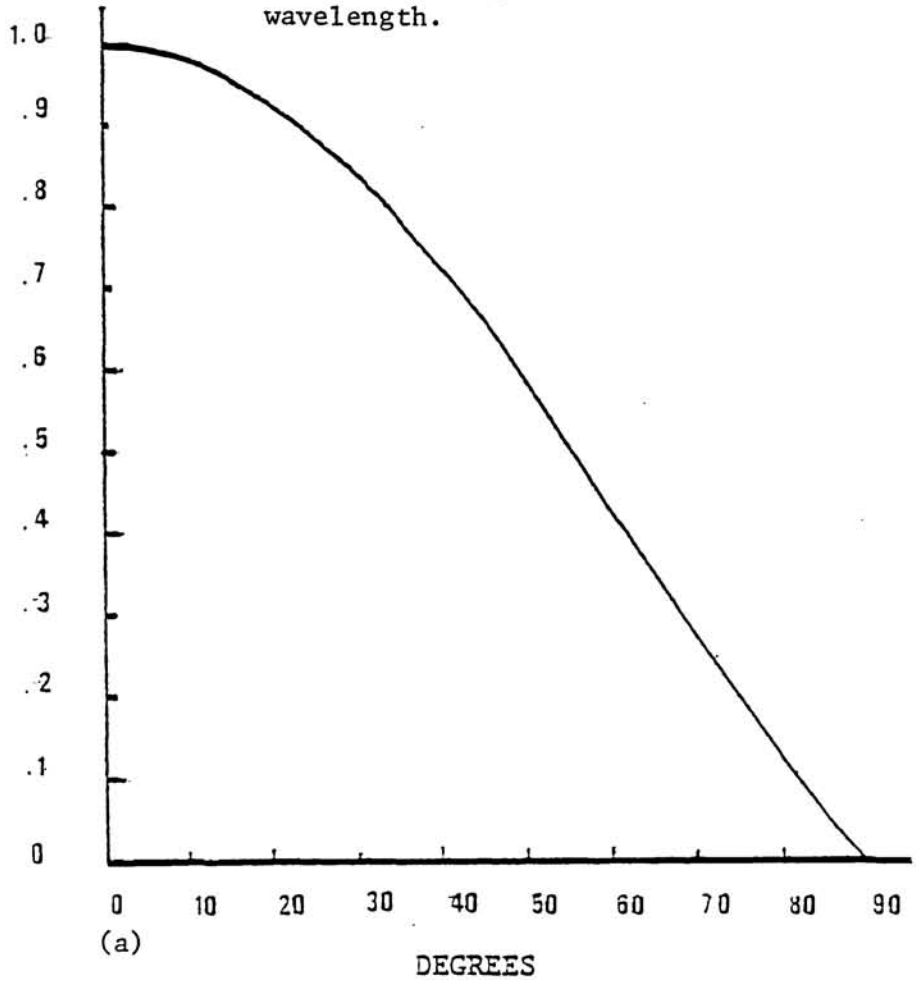
$$\frac{\lambda^2}{\Delta\lambda} > \frac{\lambda D}{r_o}$$

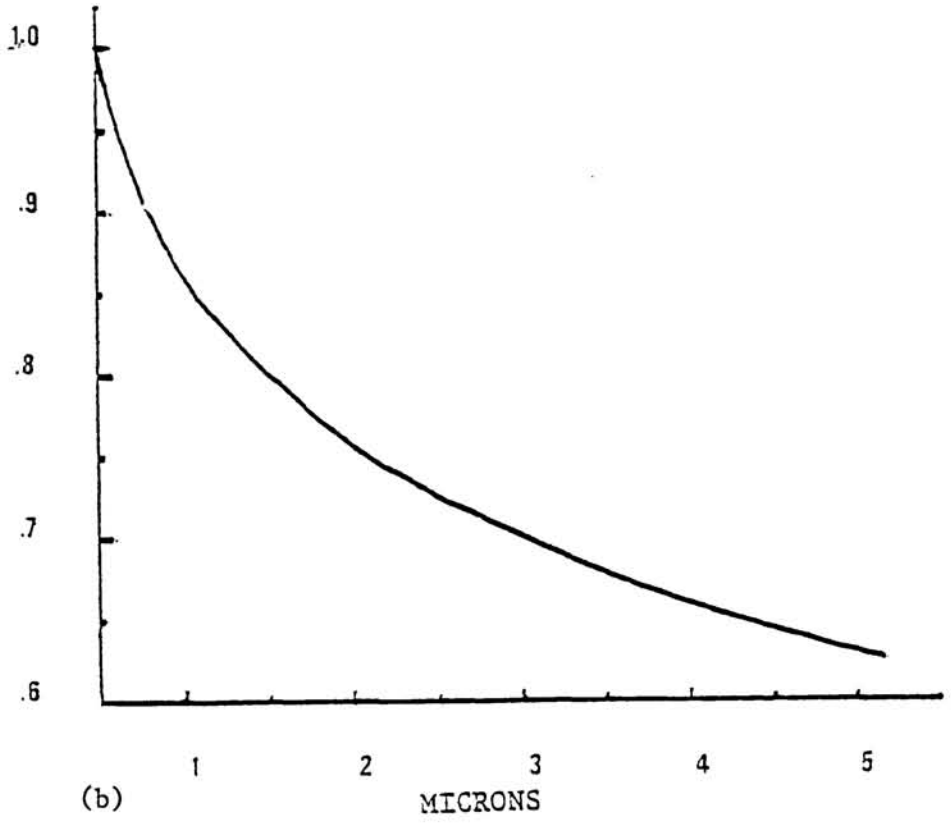
Therefore the spectral sky filter must have a bandwidth

$$\Delta\lambda \lesssim \frac{\lambda r_o}{D} \approx \frac{\lambda^2}{D\Delta\theta_s} \tag{1.26}$$

Fig.1.2 (a) Relative variation of the Fried parameter with zenith angle.

(b) Relative seeing disc size as a function of wavelength.





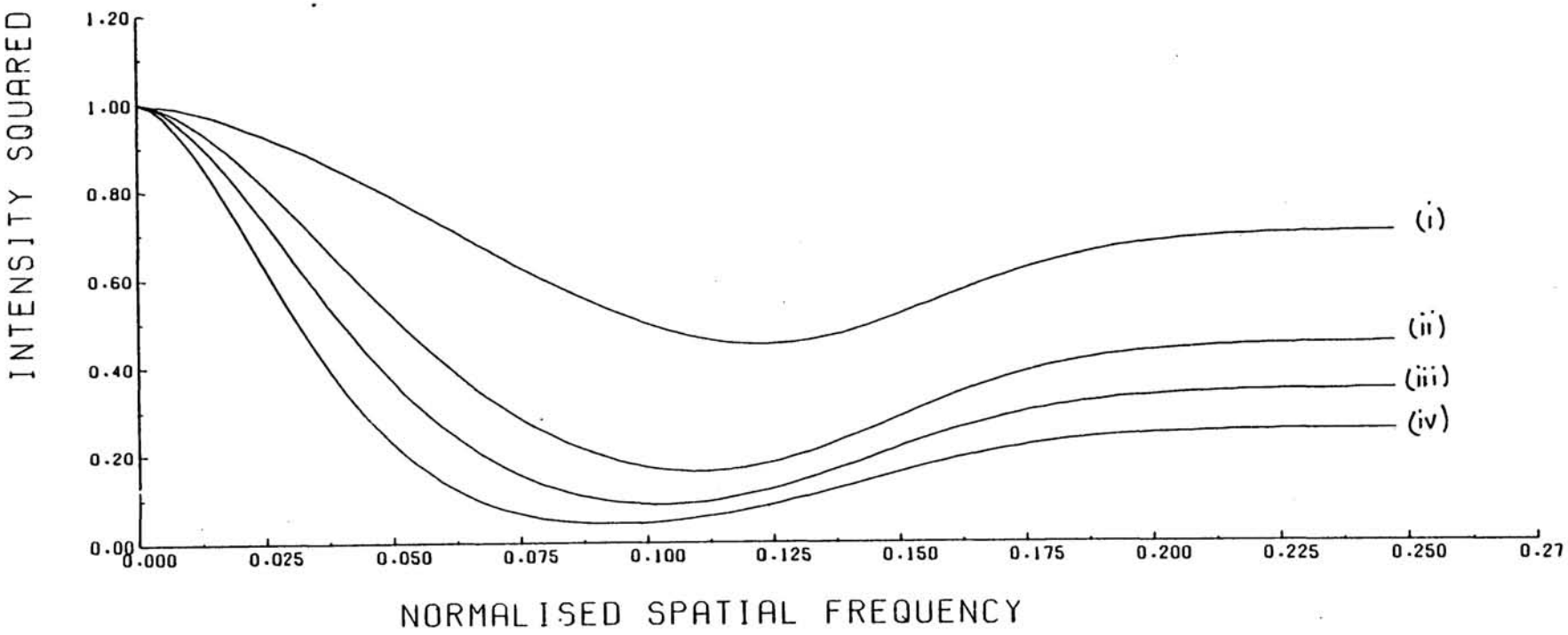


Fig.1.3. Theoretical seeing variations by division of normal model Speckle MTFs, with r_o (cm) ratios (i) 30/25 (ii) 30/20 (iii) 30/17.5 (iv) 30/15.

where $\Delta\theta_s$ is approximately the seeing angle, λ/r_o.

Tbl.1.1 shows typical central wavelengths and bandwidths for 3" seeing on a 1.5m telescope in the near infrared. Also shown is the Rayleigh resolution limit and the cut-off frequency of the telescope.

Table 1.1

	J	H	K	L	M
λ_o(μm)	1.23	1.65	2.23	3.45	4.94
$\Delta\lambda$ (3")	0.07	0.12	0.23	0.55	1.12
$\Delta\theta$ res^n.	0.21	0.28	0.37	0.58	0.83
fm (cycles /arcsec)	5.91	4.41	3.26	2.11	1.47
Dispersion	0.12	0.06	0.03	0.02	0.003

Typical spectral characteristics and limiting resolution for a 1.5m telescope in the near infrared.

1.2.2 Atmospheric dispersion

Speckle patterns observed through a finite bandwidth $\Delta\lambda$, may exhibit chromatic spreading of the higher orders due to the wavelength dependence of the atmospheric index of refraction. In the visible, the effect is large; a bandwidth of a few hundred angstroms and a compensating system are required. At near infrared wavelengths the effect is weak, the bandwidth usually being limited to maintain temporal coherence, as discussed in the last section.

An analysis of the atmospheric dispersion is given by Sibille et al. (1979) and the results obtained are shown by Fig.1.4. The figure plots attenuation of the Speckle MTF for a circular aperture for spatial frequency $\underline{f}$ parallel to the zenithal distance $\underline{z}$ in the visible (λ=0.5μm) and near infrared (λ= 2 or 5μm). For stars measured at similar zenithal distances the difference in the attenuation is only small in the 2-5 micron region.

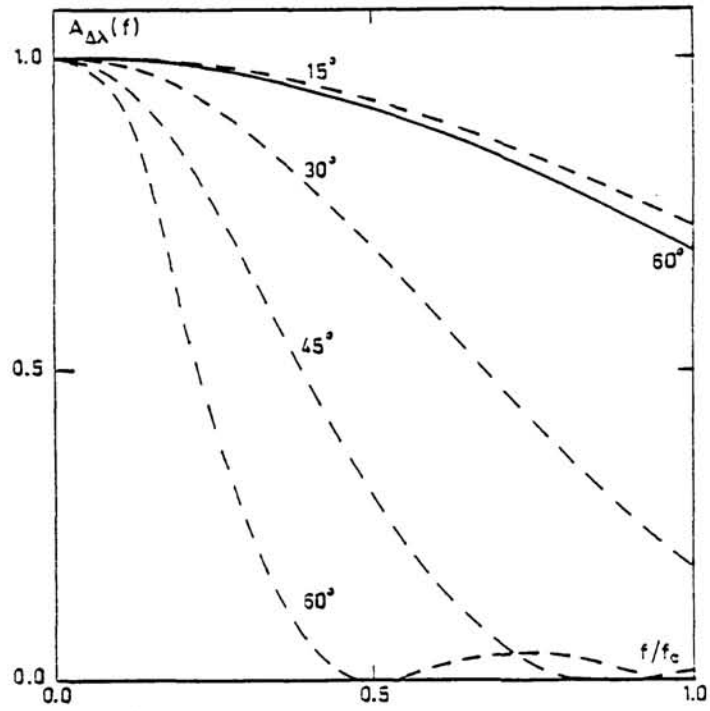


Fig.1.4 The attenuation function $A_{\Delta\lambda}(f)$. Dotted curve (----) λ=0.5μm, $\Delta\lambda/\lambda$=0.01, for z=15°,30°,45°,60°. Full curve (——): λ=2 or 5μm, $\Delta\lambda/\lambda$=0.1, z=60°.

1.2.3 Exposure time

At each spatial frequency in a speckled image there is an associated time of exposure above which speckle visibility is diminished, reducing the Speckle MTF. The critical exposure time can be thought of as a correlation time, which varies from infinity at zero spatial frequency to a value τ_c at the cut-off f_c. In the near infrared τ_c is expected to be several times larger than the value at visible wavelengths, where typical exposure times are a few milliseconds.

An analysis of the effect of finite exposure time is presented by Roddier. The quantity $I(\underline{\alpha})$ in Equ.1.1 is replaced by

$$I(\underline{\alpha}) = \frac{1}{\Delta t} \int_0^{\Delta t} I(\alpha,t)dt. \tag{1.27}$$

If the complex amplitude evolves according to a simple Taylor approximation

$$\psi(u,t) \simeq \psi(u-vt) \tag{1.28}$$

then for an exposure time ΔT the Speckle MTF reduces to

$$G(\underline{f}) = \frac{\sigma\lambda^4}{A^2} \int_-^+ \Delta(T) \int_-^+ P(\underline{u})P(\underline{u}+\underline{f})P(\underline{u}+\underline{v}\tau)P(\underline{u}+\underline{f}+\underline{v}\tau)d\underline{u}d\tau \tag{1.29}$$

where

$f_o < f \leq f_c - f_o$ and $\Delta(T)$ is the autocorrelation of the time window of duration ΔT. The right hand integral is governed by the intersection of four circles with centres at relative positions 0, $\underline{f}$, $\underline{v}\tau$ and $\underline{f}+\underline{v}\tau$. For the limiting case as $\tau \to 0$ Equ.1.20 is recovered as expected. By inspection, it is evident that the Speckle transfer function, $G(\underline{f})$, disappears when

$$|v\Delta T| \geq d \ .$$

where d is a distance smaller than the telescope diameter. The time $\Delta t_c = |v|/d$ may be thought of as the transition time from short to long exposures. Although a uniform wind of velocity $\underline{v}$ is an over-simplification, this analysis gives a useful general result and is a starting point for more detailed analysis.

1.3 Speckle limiting magnitudes

Two approaches are given in the literature for near infrared limiting magnitudes. Our Astronomy Group has determined the magnitudes for the grid method by including photometric measurements on a 1.5m telescope.

At visible wavelengths the limiting magnitude is limited by the shot noise associated with the average number of photons in a speckle. In the IR, the shot noise from the IR background is the dominant factor.

1.3.1 The Slit method

If $i_1(x)$ is the measured intensity for a given scan it is the sum of background and source contributions

$$i_1(x) = I_1(x) + B(x).$$

The statistics of signal photons (i) and speckle patterns (ii) introduce fluctuations in $I_1(x)$, whereas the photon statistics of the thermal background (iii) and detector noise (iv) cause fluctuations in $B(x)$. In the IR (i) can be neglected. The remaining processes obey Gaussian statistics.

A single scan giving a power spectrum $|i_1(f)|^2$ has a power signal to noise ratio

$$r_S = \frac{<|I_1(f)|^2>}{<|I_1(f)|^2> + <|B(f)|^2>} \qquad (1.30)$$

coaddition of N_E scans improves the ratio by a factor $\sqrt{N_E}$.

The background noise power is the sum of detector and thermal terms

$$<|B(f)|^2> = <|B_B(f)|^2> + <|B_D(f)|^2> \qquad (1.31)$$

Each of the three quantities describing Equ.1.30 can be estimated:

(i) For a point source

$$<|I_1(f)|^2> = \tau^2 N_S^2 T(f) T_S^2(f) (e\xi R)^2 / N \qquad (1.32)$$

where

$T_S(f)$ is the slit transfer function

τ the scan duration

ξ the detector quantum efficiency

R the detector resistance

and N_S the flux of photons through the slit.

The latter depends upon the photon flux from the source, N_o (photons m^{-2}, s^{-1}, μm^{-1}), the overall system transmission β, and the areas of the slit, S_s, the telescope, S_T, and the image S_I.

$$S_S = \frac{1.27\lambda}{r_o} \cdot \frac{\lambda}{2D} = 0.63 \frac{\lambda^2}{r_o D}$$

$$S_T = \frac{\pi D^2}{4} \tag{1.33}$$

$$S_I = \frac{\pi}{4} \left(\frac{1.27\lambda}{r_o}\right)^2 = 1.27 \left(\frac{\lambda}{r_o}\right)^2$$

(ii) The thermal background power generates a voltage noise across the detector

$$< |B_B(f)|^2 > = \frac{2\xi c \Delta\lambda \alpha (eR)^2 \tau E \epsilon}{\lambda^4 \left(\exp\left(\frac{hc}{\lambda k T_B}\right) - 1\right)} \; v^2 Hz^{-1} \tag{1.34}$$

where

T_B is the background temperature

ε the background emissivity

α the transmission of the cold optics

and E the beam étendue

$$< |B_D(f)|^2 > = 4kT_D R\tau \; v^2 Hz^{-1} \tag{1.35}$$

where T_D is the detector temperature.

Combining equations 1.30-1.35 the final expression for the signal to noise ratio is

$$r_S = \frac{(e\xi R)^2 . \left(\frac{S_S S_T}{S_I}\right)^2 (\beta N_o \Delta\lambda)^2 \frac{T(f)}{N} \tau \sqrt{N_E}}{4KT_D R + \frac{2\xi c E \alpha (eR)^2 \Delta\lambda \epsilon}{\lambda^4 \left(\exp\left(\frac{hc}{\lambda k T_B}\right) - 1\right)} + (e\xi R)^2 \left(\frac{S_S S_T}{S_I}\right)^2 (\beta N_o \Delta\lambda)^2 \frac{T(f)}{N} \tau}$$

for $T_S(f) \simeq 1$ (1.36)

(i) Bright sources.

If the source is bright enough for the Speckle noise term to dominate, Equ.1.36 reduces to

$$r_S = \sqrt{N_E} = \sqrt{\frac{T_o}{\tau}}$$

where T_o is the total integration time.

In this situation, τ should be chosen as small as possible whilst maintaining successive scan decorrelation.

(ii) Weak sources.

The signal to noise ratio is a strong function of r_o, (αr_o^4) and varies as $\tau \sqrt{N_E} = \sqrt{T_o \tau}$. In this case, τ should be made as large as possible whilst maintaining the short exposure régime. Sibille et al. (1979) have applied Equ.1.36 to estimate the limiting Speckle magnitudes for the slit method. Tb1.1.2 shows the results adjusted for a 1.5m telescope, calculated with the following parameters.

$D = 1.5$, $\beta = 0.4$, $\epsilon = .3$

$\xi = 0.5$, $R = 2.10^9$, $T_D = 63K$,

$T_B = 300K$, $\alpha = 0.8$, $\Delta\lambda/\lambda = 0.2$

$\tau = 100$ msec. $r_o (= 0.5\ m) = 50cm$.

$T(f) = 0.5$

Table 1.2

Wavelength	2.2	3.8	4.8
Band	K	L	M
m_{SLIT}	5.4	5.8	5.0

Slit limiting magnitudes
for a 1.5m telescope.

1.3.2 The Grid method

The limiting infrared magnitude is considered as a source whose angular extension is $\Delta\theta_D=\lambda/D$ which can be measured with a signal to noise ratio of unity.

Let $S^*(q_m)$ be the power spectrum of the extended source image at spatial frequency $q=q_m$ and $S(q_m)$ the corresponding calibration point. Here q is the spatial frequency normalised to 1 at $f= D/\lambda$.

From the normal model

$$S(q_m) = K\beta S_o D^4 T_D(q_m) \tag{1.37}$$

where S_o is the image intensity squared for a 1m telescope for the limiting Speckle magnitude. β is given by

$$\beta = (\Delta\lambda/\Delta\lambda_{ph})^2 \quad \Delta\lambda<\Delta\lambda_{ph}; \quad \text{otherwise } \beta = 1.$$

$\Delta\lambda_{ph}$ is the photometric bandwidth for the associated atmospheric window and $\Delta\lambda= \lambda^2/D\Delta\theta_S$.

The problem is to ascertain the signal to noise ratio for a signal power P_S Hz^{-1}, spread over a bandwidth ΔB, superimposed upon background noise power P_N Hz^{-1}. For the high frequency region, the bandwidth is governed by the temporal coherence in the image, $\Delta B = 1/t_o$. Generally a measurement of total noise power P with a white spectrum, over a bandwidth ΔB and post-detection integration time τ, has a signal to noise ratio $(\tau\Delta B)^{\frac{1}{2}}$. Therefore the measurement

$$S^*(q_m) = P_S \Delta B \tag{1.38}$$

has a signal to noise ratio

$$S/N \quad \frac{P_S(\tau\Delta B)^{\frac{1}{2}}}{((P_S^2+P_N^2) + P_N^2)^{\frac{1}{2}}}$$

and for a small signal $P_S << P_N$

$$S/N = \frac{P_S}{P_N} \left(\frac{\tau\Delta B}{2}\right)^{\frac{1}{2}} \tag{1.39}$$

This takes into account that in order to find $P_S\Delta B$ it is necessary to also measure the background noise power over bandwidth ΔB.

To resolve the difference between $S^*(q_m)$ and $S(q_m)$ with unity signal to noise

$$\frac{P_S}{P_N} \left(\frac{\tau\Delta B}{2}\right)^{\frac{1}{2}} = \frac{S^*(q_m)}{S(q_m)-S^*(q_m)} \tag{1.40}$$

Assuming the extended source has a Gaussian angular profile with an equivalent width $\Delta\theta_D = \lambda/D$, then

$$S^*(q_m) = \exp(-2\pi q^2)S(q_m) \tag{1.41}$$

The noise power P_N Hz^{-1} is the sum of detector (D) and thermal background (B) terms

$$P_N = P_D + \beta^{\frac{1}{2}}D^2P_B \tag{1.42}$$

P_D and P_B can be expressed in terms of photometric limiting magnitudes for a 1m telescope and a 1 second integration time.

$$\begin{aligned} M_{DL} &= 1.25 \log_{10}(S_{oo}/P_D) \\ M_{BL} &= 1.25 \log_{10}(S_{oo}/P_B) \end{aligned} \tag{1.43}$$

where S_{oo} is the zero magnitude flux squared. The resultant photometric limiting magnitude is

$$M_L = 1.25 \log_{10}(S_{oo}/(P_D+P_B)) \qquad (1.44)$$

Tbl.1.3 shows JHKLM limiting magnitudes which were calculated from measurements taken on the 1.5m telescope looking through one air mass at α Lyr, combined with fluxes of Johnson (1966). The detector noise was measured by looking at a cold (63K) metal blank. The detector is background limited at the longer wavelengths for D > 1m and partially limited at 1.2 microns.

The infrared Speckle limiting magnitude may be defined

$$M_S^* = 1.25 \log(S_{oo}/S_o) \qquad (1.45)$$

Combining Equ.1.37 to 1.45

$$M_S^* = 1.25 \log_{10}\left[\frac{(1-\exp(-2\pi q^2))T_D(q_m)\bar{r}_o^2\beta(\tau t_o/2)^{\frac{1}{2}}D^2}{10^{-0.8M_{DL}} + \beta^{\frac{1}{2}} D^2 10^{-0.8M_{BL}}}\right]$$

For background limited conditions $P_D << \beta^{\frac{1}{2}}D^2P_B$

$$M_S^* = M_{BL} + 1.25 \log(0.21\, r_o^2(\, t_o\tau)^{\frac{1}{2}}) \qquad (1.46)$$

where a value of half the cut-off frequency for q_m has been used. The value depends upon the atmospheric parameters r_o and t_o and the factor β, which is unity at the longer wavelengths. The dependence of the temporal coherence time t_o on the telescope diameter is uncertain but it may be expected to increase with diameter D.

The Speckle limiting magnitudes given in Tbl.1.3 have been calculated using the relations

$$r_o = \frac{(0.5)^{-1/5}\lambda^{6/5}10^6}{\Delta\theta_v}\ \text{m}$$

and

$$t_o = 410^{-2}\lambda^{\frac{1}{2}}\ \text{s.} \qquad \text{where } \Delta\theta_v \text{ is the visible seeing.}$$

Table 1.3

M_{BL}	15.4	15.3	14.0	10.0	7.0
M_{DL}	14.0	13.7	13.2	12.3	10.9
M_S^*	11.3	11.8	12.0	9.6	7.1

1.4 Object intensity reconstruction

The object intensity function $O(\underline{\alpha})$ for a single star can be reconstructed from blurred images only if the OTF is known. Generally, the OTF cannot be measured. However there are several possible ways in which some knowledge about the source or sources may be gained.

1.4.1 Binary star separations

Perhaps the simplest measurement from speckle images is the separation of binary stars. Labeyrie (1970) indicates that for a separation smaller than the turbulent angle, the image consists of two identical speckle patterns displaced by an amount smaller than the seeing disc. Binaries have been observed using the Speckle technique by several groups at visible wavelengths. The technique consists of co-adding infinity diffraction patterns of speckle photographs which form, in this case, a set of equi-spaced fringes whose spatial frequency is proportional to the double star separation.

1.4.2 Centrosymmetric objects

The classical Speckle method only retains Fourier amplitudes of the object and so complete image reconstruction is possible only for centrosymmetric objects. By assuming the object to be a point source plus an extended disc of diameter α_o, the data can be fitted with

$$|O(f)| = \Delta + \frac{2J_1(u)}{u}(1-\Delta) \qquad (1.47)$$

where Δ is the ratio of the power in the central source to the total power, and $u = \pi\alpha_o f$.

1.4.3 Direct Fourier deconvolution

If a point source lies within the isoplanatic patch of an object under investigation, then it may be used as an instantaneous point spread function. The object intensity distribution is then

$$O(\underline{\alpha}) = \int_{-\infty}^{\infty} \frac{i(\underline{f})}{S(\underline{f})} \exp(2\pi i \underline{\alpha}.\underline{f}) d\underline{f} \qquad (1.48)$$

The small extent of the isoplanatic patch (3") and partial isoplanatic patch (10") allows the complete reconstruction of only a small number of objects.

1.4.4 Speckles as images

The speckles of a resolved object are the convolution of the actual object intensity with a point source speckle pattern. Although for large resolved stars the speckles partially overlap, the brightest remain well separated. These can be considered as high resolution images. Location and co-addition of the brightest speckles from object and calibration images, followed by deconvolution, recovers the object function.

1.4.5 Phase of speckles

In practice, a method of image reconstruction for objects where no point source is available in the isoplanatic region is required. However, averaging the instantaneous phase in a manner similar to the classical technique for Fourier amplitude, fails. Averaging Fourier transforms of speckle images is identical to the equivalent long exposure average. This is due to high spatial frequencies undergoing phase changes that have scatter large compared to 2π. The resultant average for amplitude and phase is zero. Knox and Thompson (1974) point out that the phase difference between adjacent frequency points in speckle transforms are small compared to 2π. Therefore a time average for instantaneous phase differences should yield a non-zero result.

1.4.6 Active optics

The real time detection of atmospherically-induced phase fluctuations may be used in a feedback system to counteract the phase

changes and so reconstruct the unperturbed wave. The method therefore requires atmospheric perturbations to be detected and corrected, in a time less than 50 msec. However the phase compensation is valid only over the isoplanatic patch. Although post-detection processing is reduced, the technical difficulty of designing and constructing a working instrument is a difficult task.

Chapter 2 Techniques and Instrumentation

2.1 The Slit technique: image analysis

The stellar image spatial frequency power spectrum was measured in one dimension by scanning the seeing disc across a slit placed in the focal plane. With the slit length typically twice the average seeing disc width, the measured intensity may be written

$$I_1(x) = \int\int I(x^1,y^1)T(\frac{x^1-x}{\omega})dx^1dy^1 \qquad (2.1)$$

where T(x) is the top hat function:

$$T(x) = \begin{cases} 1 & |x| \leq \omega/2 \\ 0 & |x| \geq \omega/2 \end{cases}$$

ω is the slit width and $I(x^1,y^1)$ the two-dimensional image.

The power transform of Equ.2.1 yields

$$<|I_1(f_x)|^2> = <|I(f_x,0)|^2> t_s^2(f_x) \qquad (2.2)$$

where

$$t_s(f_x) = \frac{\omega \sin \pi\omega f_x}{\pi\omega f_x}$$

The measured power at spatial frequency f_x is a function of the slit width and its maximum value may be obtained by solving the equation

$$\frac{\delta}{\delta\omega}\left[\frac{\omega\sin(\pi\omega f_x)}{\pi\omega f_x}\right] = 0$$

The required relation is $\omega = 1/2f_x$. I chose to maximise the power at the cut-off frequency f_c. Tbl.2.1 shows the experimental slit widths and also the spectral filter parameters.

The image was scanned back and forth using a triangular motion of chop amplitude a arcsec and frequency f_{ch} Hz, so that the plate

scale speed was

$$R = 2af_{ch} \text{ "s}^{-1} \tag{2.3}$$

Spatial frequency f_s(cycles/") then translated to temporal frequency f_t:

$$f_t = Rf_s \text{ Hz.} \tag{2.4}$$

The chop amplitude was typically 10". Once chosen, along with the temporal cut-off frequency, the chop frequency could be evaluated.

It is important to note that two methods exist for estimating the background power, $\langle |B(f_x)|^2 \rangle$. Provided accurate guiding is possible, $\langle |B(f_x)|^2 \rangle$ can be assessed adjacent to the source and alternately with the speckled image. The alternative approach is to make measurements of the source and background separately, provided the infrared background is not varying.

Table 2.1

	K	L	M
λ_o	2.26	3.83	4.82
$\Delta\lambda$	0.22	0.14	0.18
a(μm)	15	26	33

Experimental spectral filters and slit widths

2.1.1 Signal processing

Fig.2.1 shows the analogue system used for the first Slit Speckle measurements in August 1979. At the time, the performance of the system in faithfully recording the information was unproven. Not until the development of the full data reduction software was the performance appraised. In fact a combination of factors worked against the high resolution technique, particularly at the shorter wavebands, J, H and K. These were

1) The bandwidth of the preamplifier, $1/R_fC$ where R_f is the value of the feedback resistor and C the stray capacitance across it.

2) The form of the Speckle MTF itself, having a flat low valued high

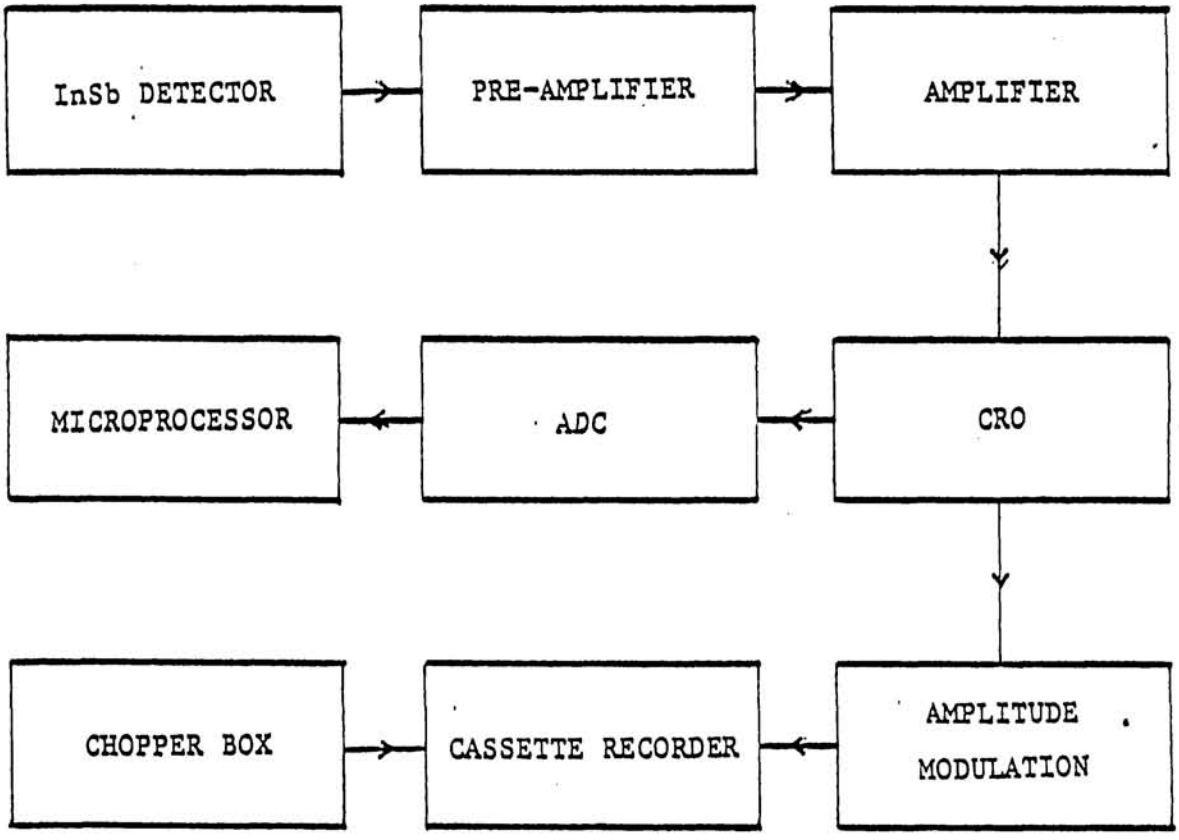


Fig.2.1 Speckle data acquisition and on-line analysis (1)

frequency tail.

3) The amplitude modulation was later discovered to have a monotonically decreasing electrical MTF.

The signals were tape recorded. The higher frequencies which were reduced in amplitude were then subjected to tape noise, and so the angular resolution was reduced.

The system has been modified. A 'roll up' amplifier provides extra gain for frequencies in the range 50-500 Hz before cutting off sharply. This allows the signals to be safely tape recorded, reduces noise and avoids aliasing in the later digital reduction. The cassette recorder was replaced by an SE Labs. 3500 FM tape recorder. This has 8 recording channels and variable bandwidth. A voice channel can be used to identify scans. Fig.2.2 shows the modified system.

One aspect of such electrical systems hitherto unmentioned is that of pick up. The high, dry mountain site in Tenerife does not have an adequate earth and the result has often been 50 Hz pick up. The problem is currently being addressed, e.g. single earth systems using optical isolation to prevent earth loops.

2.1.2 Data analysis

A Laboratory analysis

The data reduction divided into four tasks:

(1) Analogue digitisation

The minimum digitisation rate is

$$f_D = 2Rf_{s_{max}} = 2f_{t_{max}} \qquad (2.5)$$

but can only be approached if the signal is adequately low pass filtered. If the seeing disc is scanned so that its duration corresponds to T seconds, the number of independent points is

$$n_I = Tf_D = 2\Delta\theta_s/\Delta\theta_D \qquad (2.6)$$

$\Delta\theta_s$ is the seeing width and $\Delta\theta_D$ the telescope resolution.

The Interdata 70 (see section 2.4.2) processor was dedicated to digitisation by status looping on

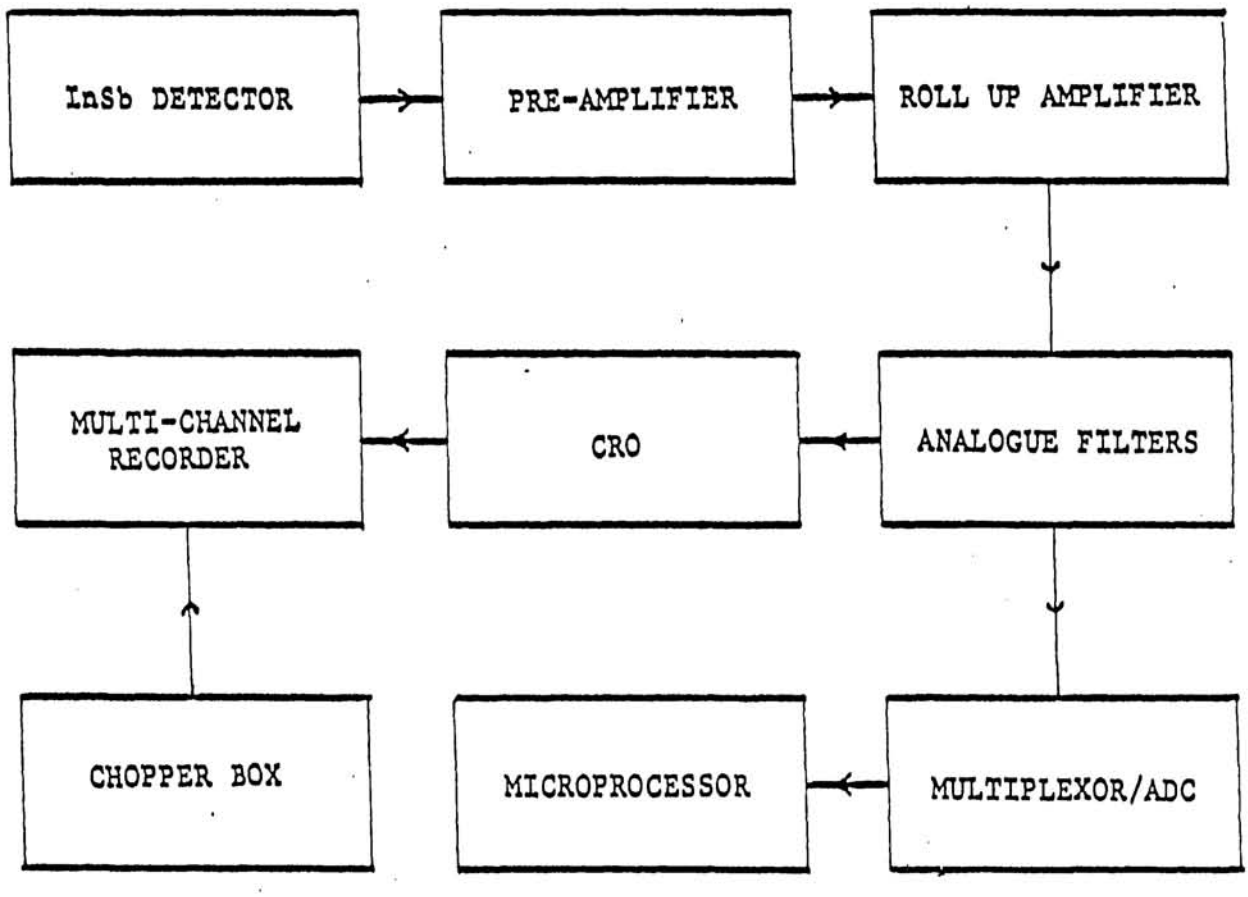


Fig 2.2 Speckle data acquisition and on-line analysis (2)

(i) a trigger pulse marking the start of each scan

(ii) the analogue to digital converter (ADC) status.

The digitisation rate was determined by a TTL pulse generator which provided trigger pulses for the 10 bit ADC module. The maximum conversion rate was software limited at 900 samples per second, adequate for signals obtained on a 1.5m telescope. Three hundred scans, stored in 512-word blocks, were written to disc per digitisation run.

(2) Background and Source Power Transformation

Each image scan was divided into source and background power parts and from each the background level was removed. Fifty such scans were taken together to estimate power transforms of the source $<|I(f)|^2>$ and background $<|B(f)|^2>$ parts. They were calculated by coadding fifty scan autocorrelations and then cosine transforming the result. Finally the background power spectrum was subtracted from that of the source.

The algorithms

The scan signal may be written

$$i(t) = I(t)\Omega(t/\tau) \tag{2.7}$$

where $I(t)$ is the infinite scan and $\Omega(t/\tau)$ the time window of duration τs. I approximated the autocorrelation function

$$C(\tau) = <I(t)I(t+\tau)> \Lambda(t/\tau) \tag{2.8}$$

with

$$C(m) = \sum_{n=0}^{N-1} I(n)I(n+m) \tag{2.9}$$

Similarly the power transform

$$P(f) = \int_{-\infty}^{\infty} C(\tau)\cos(2\pi f t)dt \tag{2.10}$$

was estimated using

$$P(k) = \sum_{m=0}^{N-1} C(m)\cos(Ak,m) \tag{2.11}$$

where $A = 2\pi\Delta f\Delta t$, $\Delta f = f_m/k_m$

and $\Delta t = 1/2f_m$

(3) Object spectrum recovery

Interactive execution was necessary to plot power transforms and spectra on a TEKTRONIKS terminal in order to reject and select transformations. Power transformations from a given source with similar seeing judged by the flatness of a power ratio were added to improve signal to noise. Outstanding power spectra could be plotted and compared with the associated background spectrum. Several recovered spectra for one object, or a calibration ratio, would be combined, normalised to DC and punched on paper tape for the final task.

(4) Graphical plotting

I have developed several Fortran programmes on the ICCC time-sharing system. These plotted recovered spectra against two component source models (Equ.1.47) or ratios of Speckle MTF's with different Fried parameters (see Fig.1.3). The plots were viewed on a TEKTRONIKS terminal and hard copies saved on microfilm.

B On-line analysis

Partial analysis at the telescope is essential to determine the state of the atmosphere and the angular size of the source. To determine the source's extension, it is necessary to measure the

(i) infrared seeing

(ii) signal to noise as a function of spatial frequency, and

(iii) to look for a correlation between the seeing width squared and the high frequency Speckle power.

The last point is very important. Atmospheric seeing effects have to be recognised and separated from the measurements of the extended source. Mike Selby and I have tried two approaches to the problem: (i) a purely digital and (ii) a hybrid analogue-digital method. The two reflect different ways of measuring the background power.

The digital method was a miniature version of the full analysis package with much of the programme written in assembler. However, the development of the reduction technique was still in progress and so only limited results were forthcoming.

More recently, the analogue-digital approach was adopted as a method of compressing incoming data to ease the treatment of all scan signals. The system consisted of a bank of bandpass filters (see section 2.4.1) which sampled the Speckle MTF. Provided adjacent images

did not overlap, the outputs were proportional to the r.m.s. power in the signal, over the filter bandpasses. The analogue signals were then multiplexed and reduced on an AIM 65 microprocessor system.

2.2 The Grid technique: image analysis

The time-averaged spatial frequency power spectrum of the instantaneous image I(x,y) was sampled in one direction by sequential use of spatial frequency transmission gratings (grids). With a filter in position, the image was oscillated across the grating, normal to the grating lines (as in the slit technique). The signal detected was modulated at a quasi constant frequency, typically 120 Hz, which is convenient for the electrical bandwidth of the system, and this allowed the image to remain frozen over several periods of oscillation. The image motion was again pre-programmed for constant amplitude and varying chop frequencies.

Given the one-dimensional image intensity $I(x^1)$ at position x^1, the detected signal is

$$S_{f1}(x^1) = I(x^1) * (G_{f1}(x^1).A(x^1)) \qquad (2.12)$$

where $f^1 = 1/S^1$, the grating constant.

The transfer function of the transmission grating is

$$T_{f1}(f) = g_{f1}(f) * a(f) \qquad (2.13)$$

where $g_{f1}(f)$ and $a(f)$ are Fourier transforms of $G_{f1}(x^1)$ and $A(x^1)$.

If $G_{f1}(x^1)$ is assumed to be $\cos(2\pi f^1 x^1 + \phi)$ where ϕ is an arbitrary phase factor, the filter $T_{f1}(f)$ is peaked at $f = \pm f^1$ with an equivalent width $\Delta f \simeq \pi/b$. For $b >> f^1$ $\Delta f/f^1 << 1$ and is approximately

$$S_f(x) = i_a(f^1)\cos(f^1 x^1 + \phi + \Phi(f^1)) \qquad (2.14)$$

where $i(f^1) = i_a(f^1)\exp(j\Phi(f^1))$ is the Fourier transform of I(x).

If $I(x^1)$ is constant in time, the mean power of $S_f(x^1)$ is proportional to the spatial frequency power per unit bandwidth $i_a^2(f^1)$, averaged over infinite x^1. However the finite chop amplitude leads to a systematic error in the assessment of $i_a^2(f)$ dependent upon ϕ, $\Phi(f)$ and

a. The errors are tolerable for the finer gratings but the use of the coarser gratings required an increase in chop amplitude (a).

2.2.1 Signal processing and data analysis

The spatial frequency power spectrum is sampled separately by the Grid method and so the rigorous demands imposed by the slit method concerning data acquisition and processing do not apply. For example, the electrical MTF need not be 'flat'. Measurements are all made in the AC mode with digitisation rates of only 400 samples per second. Data analysis was developed on an Interdata 70 minicomputer (see section 2.4.2).

2.3 Observational technique

The observations require three observers to guide, operate the on-line analysis and to tape record, note the observations and do system selections. An interesting object should be measured with two or three calibration stars if possible. If the background is monitored separately from the source, it is measured before and after each source to check for variations. System selections during the observations are

(i) Spectral and spatial filters

(ii) Preamplifier feedback resistor

(iii) Chop frequency f_{ch}

(iv) Amplifier bandwidth.

The plate scale speed, chop amplitude and bandwidth on the FM recorder are selected beforehand. During each measurement the sidereal time is noted to calculate the air mass from the standard relation

$$\sec z = (\cos\lambda\cos\delta\cos(HA)+\sin\lambda\sin\delta)^{-1} \qquad (2.15)$$

where λ is the latitude

δ is the declination

HA is the hour-angle and is given by

HA = sidereal time - right ascension.

2.4 The Observational system

Most observations reported in this thesis have been taken on the 1.5m flux collector at Tenerife. The telescope is situated at $28^{o}17^{1}32^{"}$ latitude, 1h 5m 48.1s longitude, at a height of 2500m. The absolute pointing was only ±5' and so a small finder telescope facilitated locating objects. Offsetting motions were accurate to $30^{\hat{n}}$ so that invisible objects could be found from nearby visible stars. The telescope's maximum zenith viewing was 67^{o}.

The ground-based infrared user system was designed for use at the telescope's Cassegrain focus. The second beam was turned through 180^{o} by a 2-mirror focal plane chopper, situated below the photometer cage. The chopper was driven by control electronics, capable of supplying and servoing triangular or square waveforms, pre-programmed if necessary. The focal plane for the arrangement lay 5.4 inches above the photometer baseplate and the resultant plate scale was $10"mm^{-1}$.

Fig.2.3 shows the internal configuration of the Speckle cryostat, designed to operate on the 1.5m flux collector (F.C.). The principal cold aperture was situated 3 inches distant from the focal plane and selected an F12.5 beam. The detector, field optics, spectral and spatial filters were all cooled to either liquid nitrogen temperature (LNT) or pumped LNT. The latter temperatures were maintained by means of a mechanical servo attached to the cryostat on one side and a rotary pump on the other. The spectral and spatial filters sat in separate wheels, which could be positoned externally, to give the required filter combination. To ensure exact positoning, a warning LED extinguished when the wheels were correctly located.

A zinc selenide field lens, situated behind the focal plane, focussed the primary mirror onto the detector. Its primary use was to reduce the effects of guiding errors.

The lens focal length was measured in the visible and suitably adjusted using the paraxial approximation, for the infrared image. A 0.5mm InSb detector supplied by Santa Barbara Research Corporation was used and operated in the photovoltaic mode.

Gratings and slits were made by microprocessor-controlled laser cutting of Molybdenum foil (1^{th} thickness). The apparatus consisted of a commercial Neodymium YAG laser and a translator driven in two perpendicular directions by precision stepping motors. Each filter was made as a series of cuts and spaces: the former ranged from 5 to 100

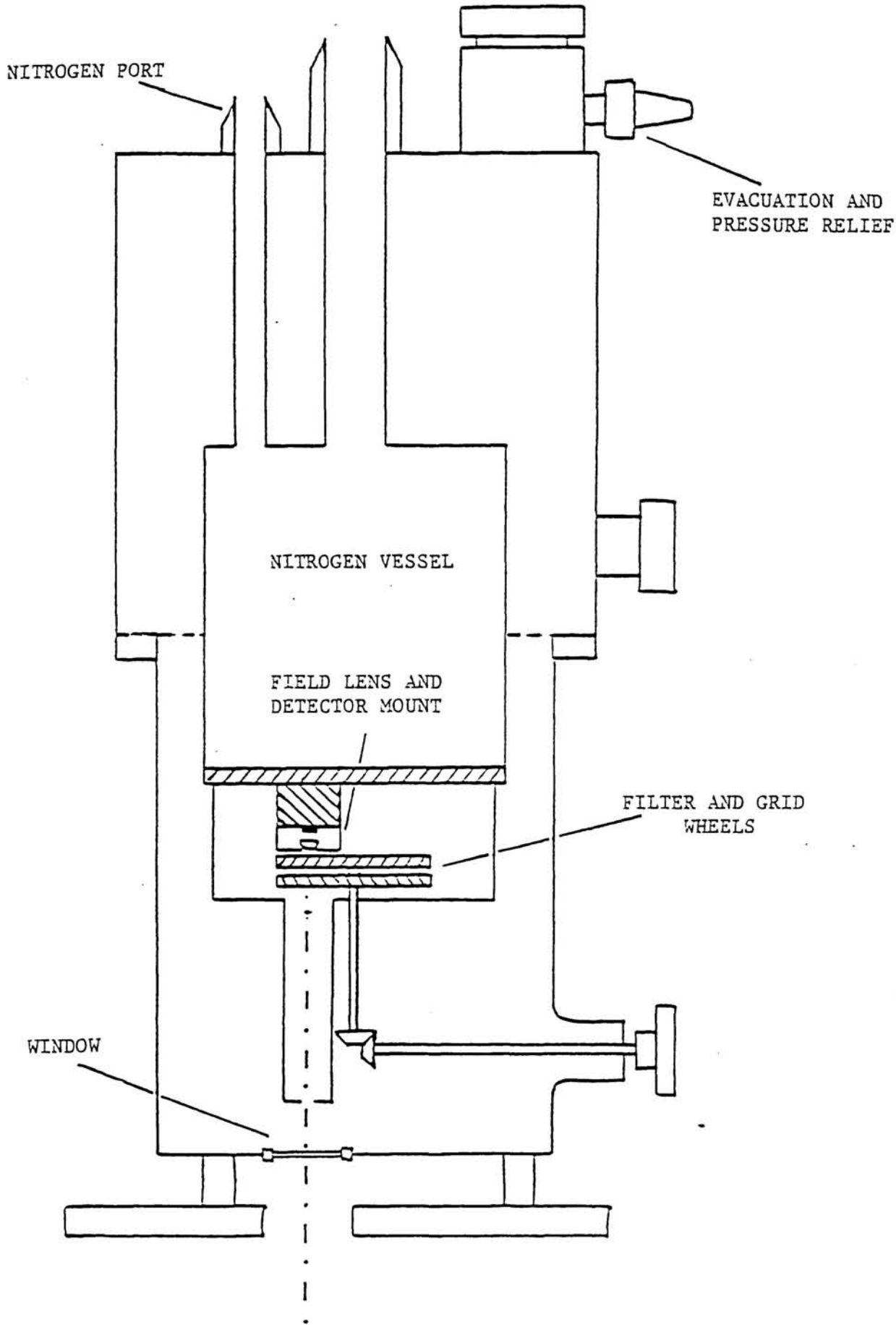


Fig.2.3 The Speckle Cryostat

microns width and an integral number of 1.25 microns length. Cuts were made at 60 microns s^{-1} and the process was viewed through a microscope arrangement.

An alternative process for making grids was attempted by the group and subsequently by Graticules Ltd. This involved photo-resist processing and chemical etching of chromium-coated sapphire discs. The method proved particularly good for the finer grids.

2.4.1 Analogue electronics

A. Preamplifier

Fig.2.4 shows the InSb preamplifier circuit developed by Dr A.D. MacGregor in 1976. The circuit is designed to achieve Johnson noise-limited InSb operation, with a basic design philosophy that detector current be forced through a feedback resistor. The output voltage is measured in an AC or DC mode.

In the absence of radiation the detector exhibits the characteristics of a normal diode, with an associated leakage resistance R_D. A high value for R_D is desirable in order to decrease the Johnson noise current:

$$i_n = (4kT/R_D)^{\frac{1}{2}} \text{ A Hz}^{-\frac{1}{2}} \qquad (2.16)$$

The detector resistance is measured whilst the detector views a cold metal blank, by varying the voltage across the detector V_D by means of SW1 and monitoring the output voltage V_o. For the linear part of the diode curve

$$R_D \approx \frac{V_D}{V_o} \cdot R_L \qquad (2.17)$$

where R_L is the feedback resistance.

The feedback resistor can be selected by the latching relay LR1, to avoid saturating the preamplifier under high background conditions ($R_L=10^8\Omega$), whilst allowing InSb Johnson noise-limited operation under low background situations ($R_L=10^{10}\Omega$). The bandwidth is limited by the parallel capacitance across the feedback resistor. It is of the order $1/R_L C_L$ and for $R_L = 10^{10}$ ohms the half power point is about 50 Hz (see Fig.6.3b).

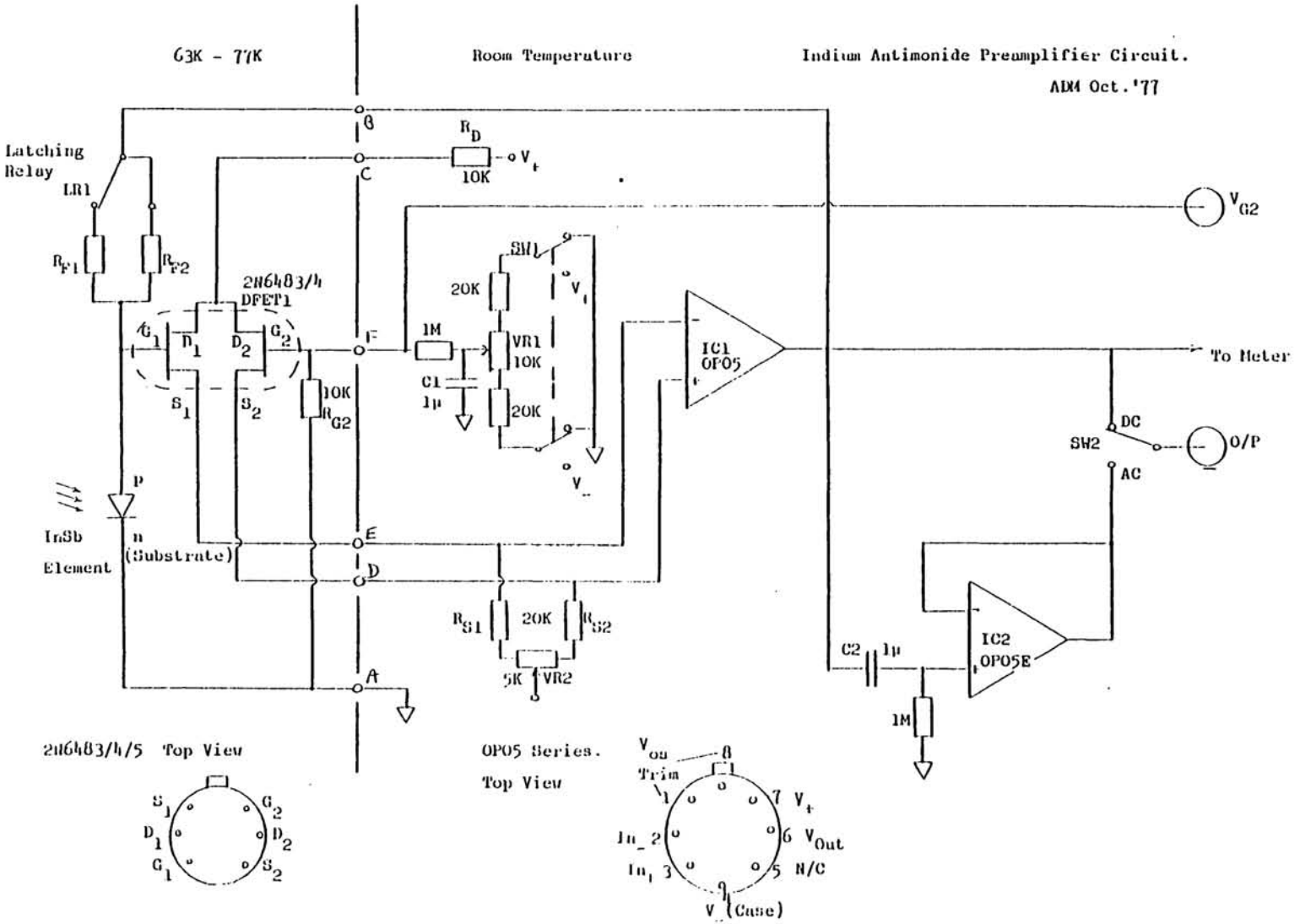


Fig.2.4 The InSb preamplifier

B. Roll up Amplifier

As discussed in section 2.1.1 a roll up amplifier was designed to improve the response for frequencies in the range 50-500 Hz. Fig.2.5 shows the design. The input stage allows large background offsets to be removed by application of a voltage to the non-inverting input. The gain as a function of frequency is controlled by the capacitor c* and this stage is selected for $R_L = 10^{10}\Omega$. The amplification stage provides gain over a five decade range.

† see fig 6.3

C. The analogue filter bank

The arrangement of analogue filters designed for the on-line data reduction is shown in Fig.2.6. Bandpass and cut-on/off filters were applications of basic designs given in Burr-Brown (1971). The primary low pass and the high pass filter which prevents leakage of the Speckle MTF low frequency peak into the high frequency region were 8-pole Butterworth filters. Channels 2-5 were designed as narrow band filters with Q's of about 10; channels 3-5 were tunable; channels 1 (DC) and 6 (integrated Speckle power) completed the filter bank. The outputs of each filter stage were fed into r.m.s. chips and post detection amplification supplied useful dynamic ranges for the following ADC. Each channel was capable of a single power measurement to better than 1% over integration periods of several seconds.

2.4.2 Digital electronics

A. The AIM 65 classical micro-system

Both instrument control and on-line data analysis have been revolutionised by the recent advances in silicon chip technology. I have developed a classical microprocessor system, based upon Rockwell's 6502 microprocessor, previously only achievable with expensive minicomputers. A schematic diagram is given in Fig.2.7.

Two factors influenced the choice of processor: (i) the supplied keyboard, printer and display and (ii) the low cost (the 1K version is £285). Although the 6502 microprocessor chip is not sophisticated, the system software provided has helped establish the product.

AIM 65 is an 8-bit microprocessor with a 16-bit address bus. In addition to the standard MONITOR read only memory (ROM), I have implemented BASIC and ASSEMBLER ROM's. The 4K bytes (1 byte = 8 bits) of read-write memory (RAM) have been supplemented by CUBIT (4K bytes) and memory plus (8K bytes) boards. The latter can address 8K bytes of

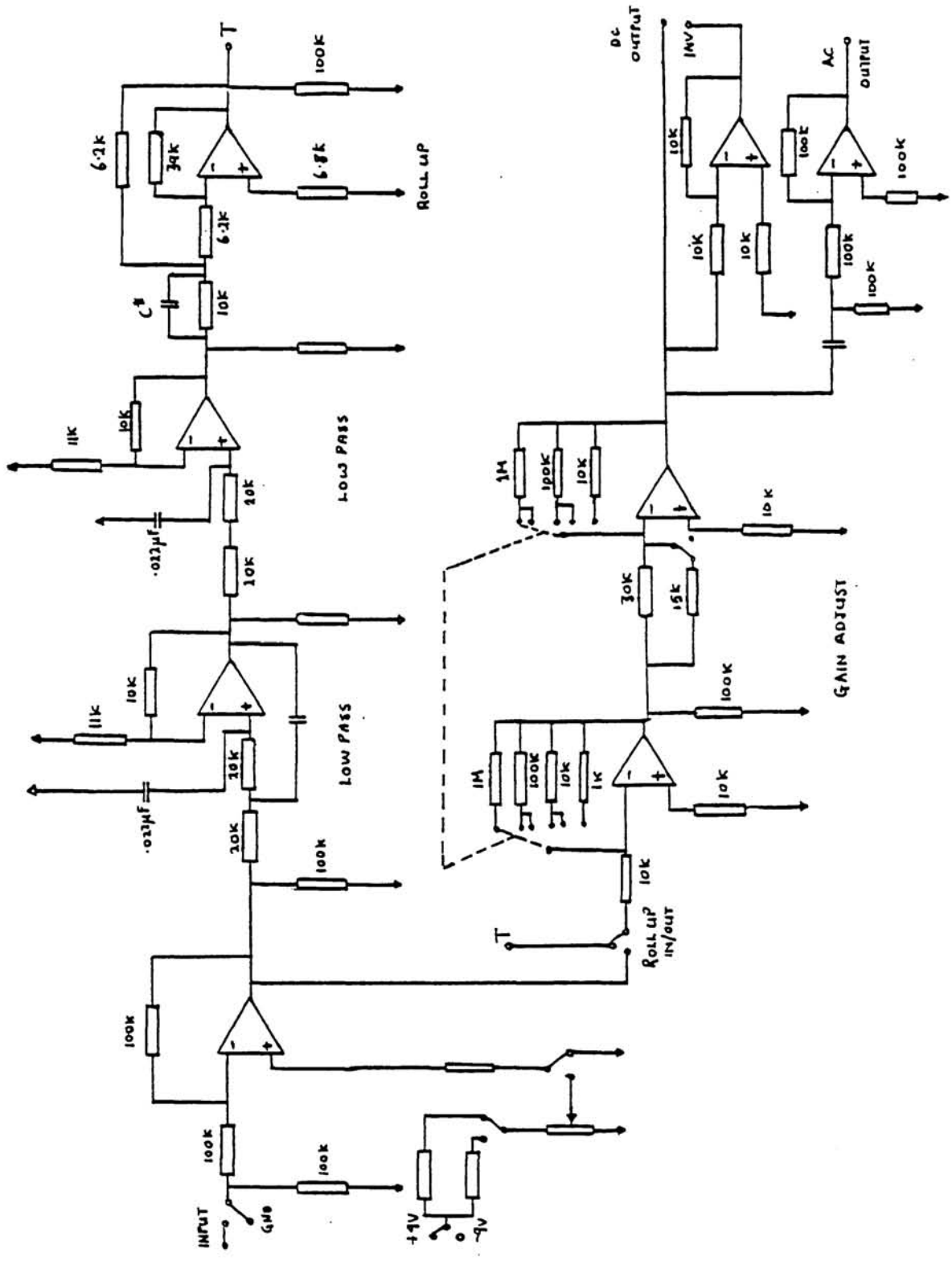


Fig.2.5 DC roll up amplifier

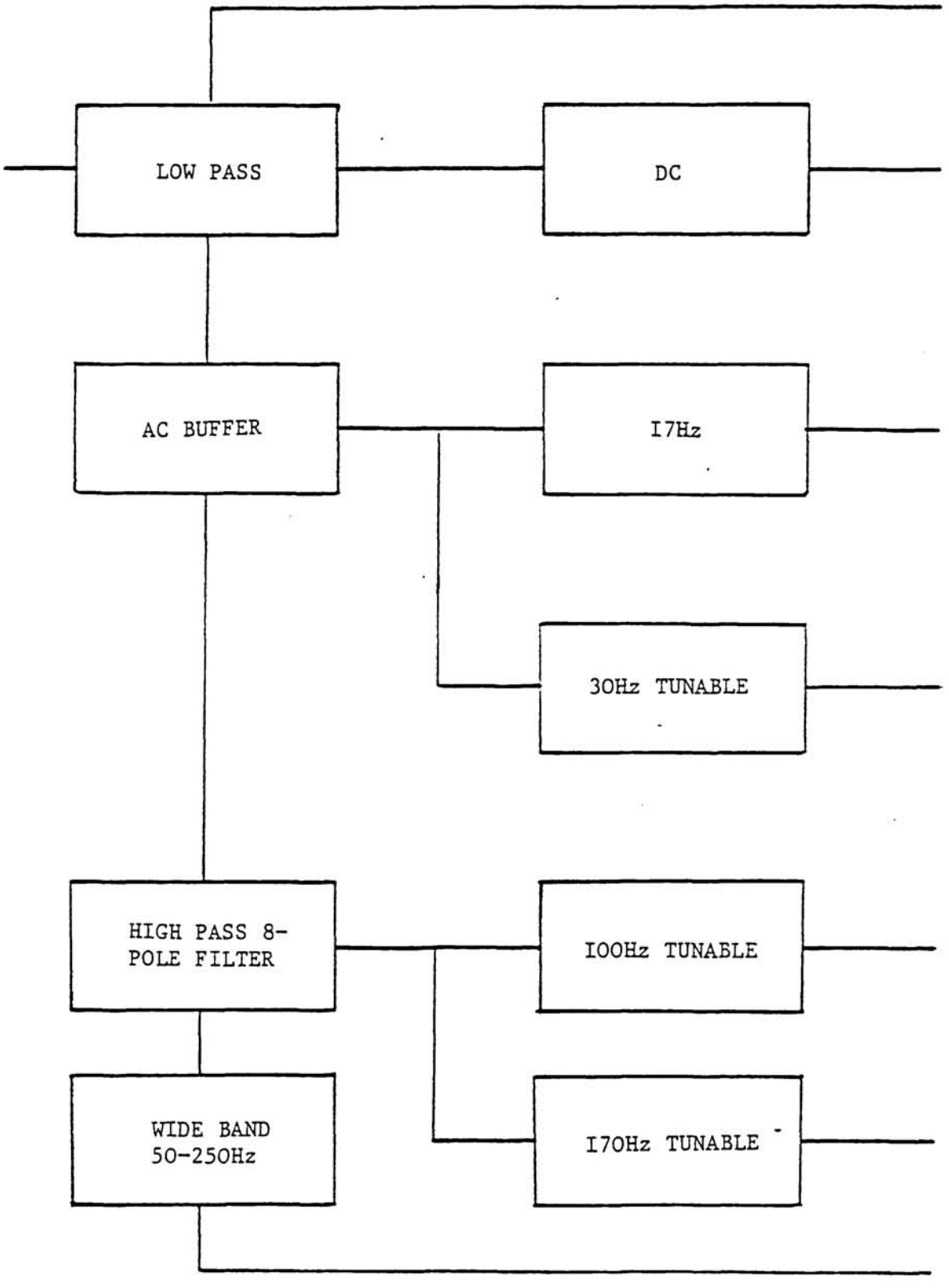


Fig.2.6 Analogue filter arrangement

ROM and has a programmable ROM (PROM) burner - a device for creating PROM's.

Programme development was improved at all language levels by an external current loop to RS 232 interface, enabling a VDU and line printer to be used. Large low level programmes were developed with the aid of the assembler programme, which allowed user programmes to be edited and compiled.

External circuitry was designed and built around Vero Electronics' KM6 racking system and Eurocard component boards. Modules are either addressable or dedicated to one of the three versatile interface adaptors (VIA).

One such dedicated module was the multiplexor/ADC, designed to follow the analogue filter bank described in the previous section. Fig.2.8 shows the circuit. Three output port lines selected one of eight analogue inputs for the ADC chip. The analogue signal accepted could be uni- or bi-polar. The full dynamic range was 5.5 volts and an 8-bit conversion took 3 microseconds. The result could be coded as offset binary or 2's complement.

B. Interdata 70 and Forth

The Interdata 70 was formerly the Astronomy Group's minicomputer. The processor had a 16-bit word length and addressed 32K words of memory. It was equipped with a CAMAC interface and peripherals included VDU, Tektroniks and line printer.

The computer was used to analyse slit Speckle data through default. The alternative processor was the ICCC mainframe. However there was no method of digitising and transferring large quantities of data to the ICCC network.

The programming language was Forth. The advantages of Forth were that it occupied a relatively small region of memory and executed relatively quickly. Furthermore, many routines already existed. The problems encountered were that transformations were tedious to write in Forth and theoretical modelling impossible due to a void of many trigonometrical functions. Furthermore the processor was frequently inoperative as a result of its long service, and eventually a disc drive failed irreparably prior to the completion of all the Speckle analysis.

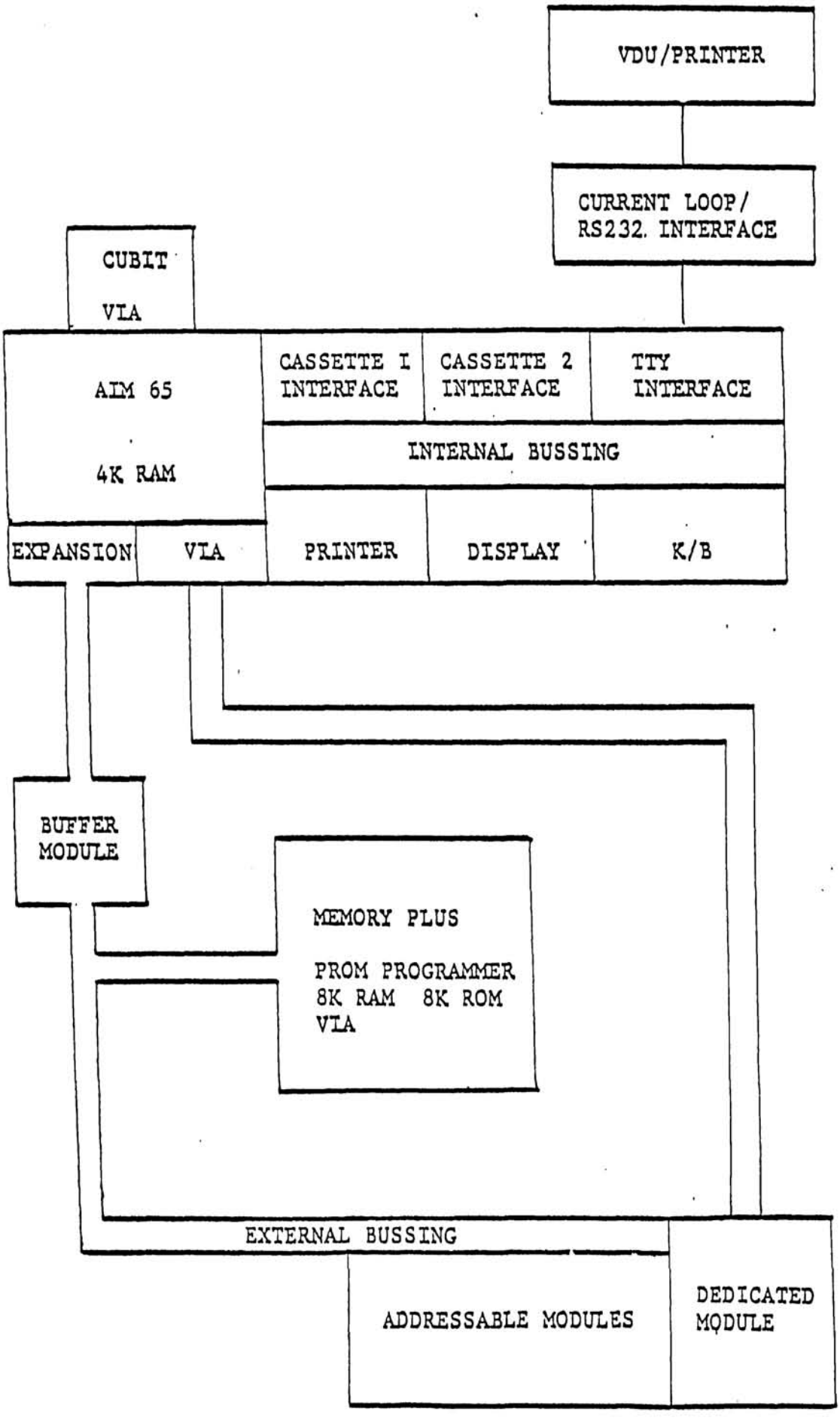


Fig.2.7 Classical microprocessor system

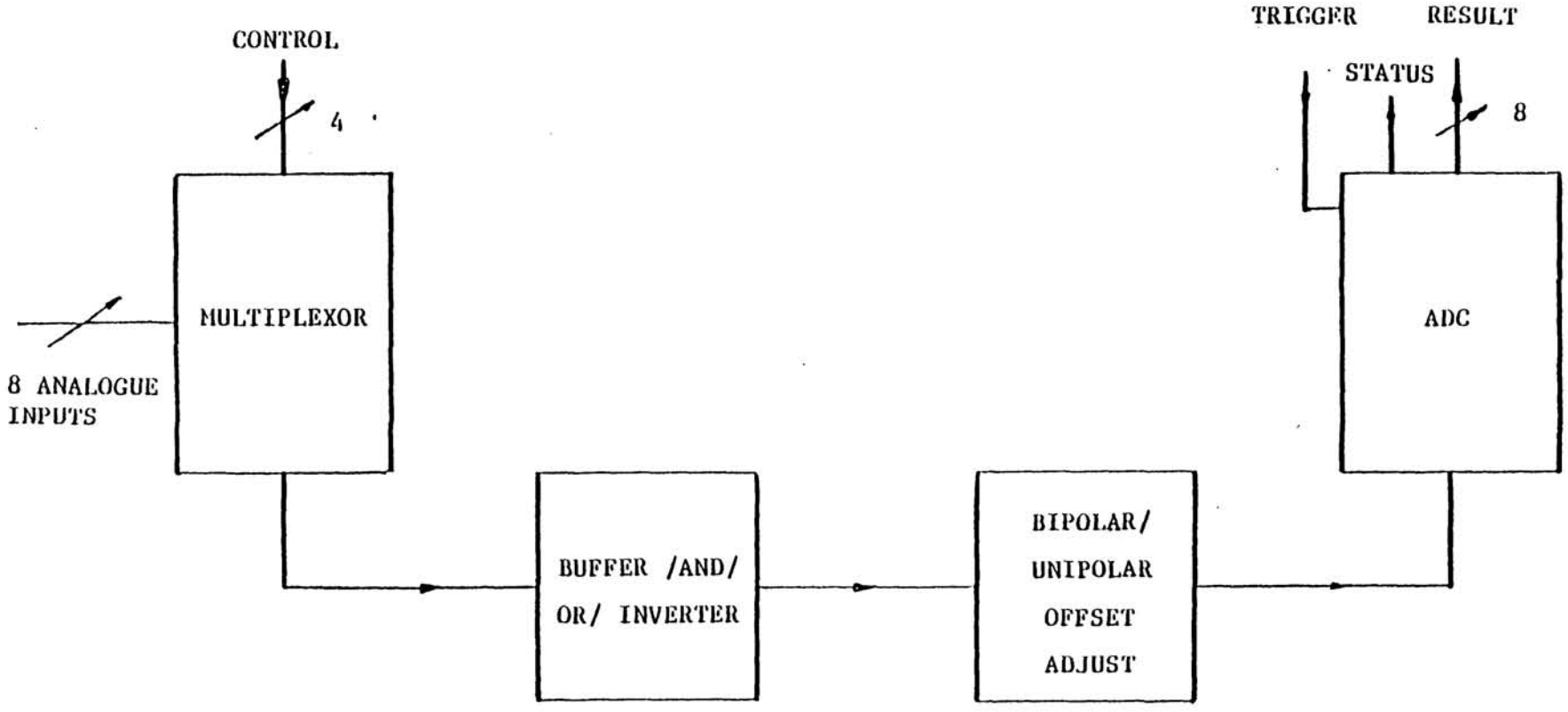


Fig.2.8 The multiplexor/ADC module

Chapter 3 Results

3.1 Introduction

The low resolving power of the 1.5m flux collector restricts the number of IR stars with circumstellar shells which are resolveable. This is evident after measuring several early and late type objects, including CIT6, VYCMa and IRC+10216, all catalogued in the two micron survey, and also the protostellar object GL2591.

The 'two micron' objects have been measured using the grid technique and more recently with the slit technique. Only IRC +10216 is clearly resolved. GL2591 was measured at 3.8 microns using the slit technique and found to be unresolved. Foy et al. (1979) found the object to be unresolved ($\lesssim$ 70 m arcsec) at 3.5 microns.

For the slit technique much of the observational data was rejected at the power transform stage due to either windbounce or guiding errors shifting the image in the scan time window (about half the objects attempted were invisible). Variable seeing also resulted in power transform rejection. Recovered spectra represent about 10% of the original data.

A further measurement, Io, the third largest Galilean satellite, measured on the 3.8m UKIRT, is also reported.

3.2 Results

(i) Grid

Fig.3.1 shows the recovered power spectrum of the late type carbon star IRC +10216 at 2.2 microns. The stability of the atmosphere during observation of the source and calibration is measured by the calibration ratios (those points including error bars). The mean was taken of the normalised spectra of four calibration stars and each power spectrum was divided by this mean so that the spread represents the change in the atmospheric MTF over the observational period. We have fitted the data with a Gaussian profile of equivalent width 0.35". (The equivalent width is that width of a unity height top hat function of the same area.)

Other grid measurements were made in January 1979 but the variation

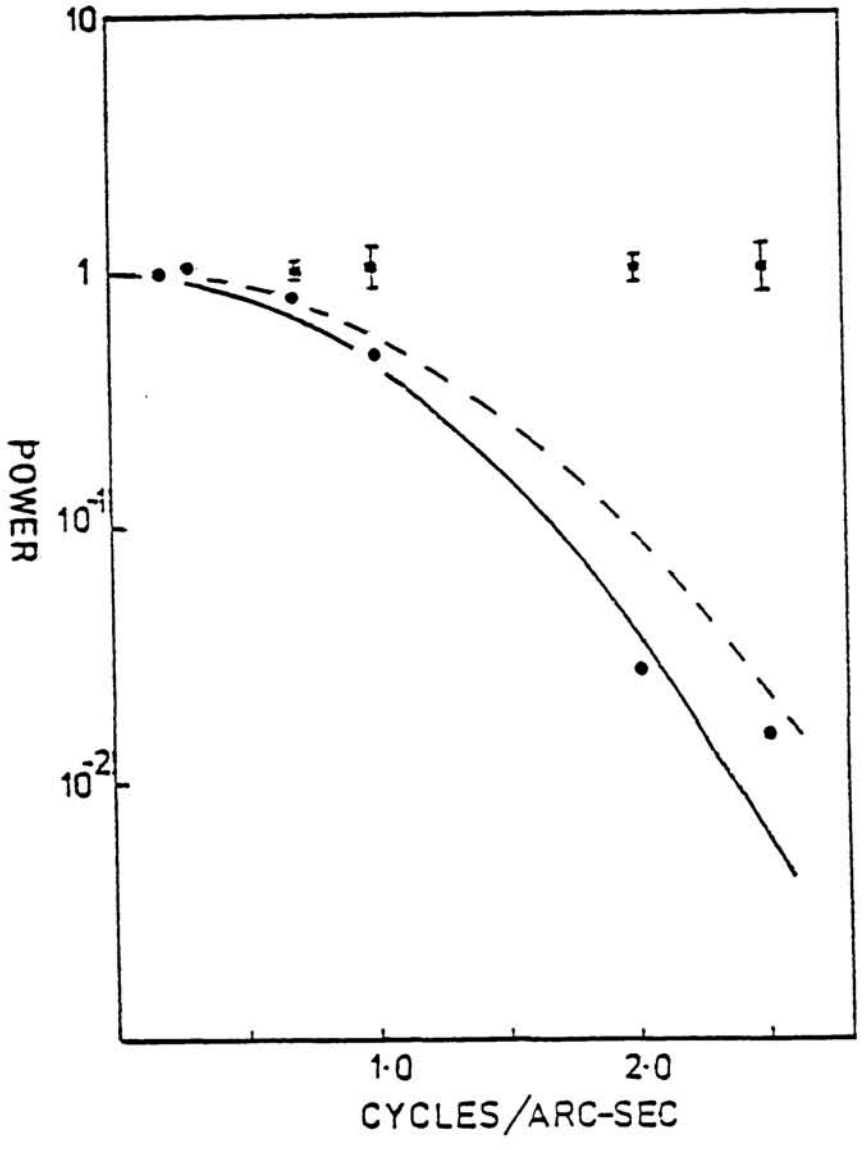
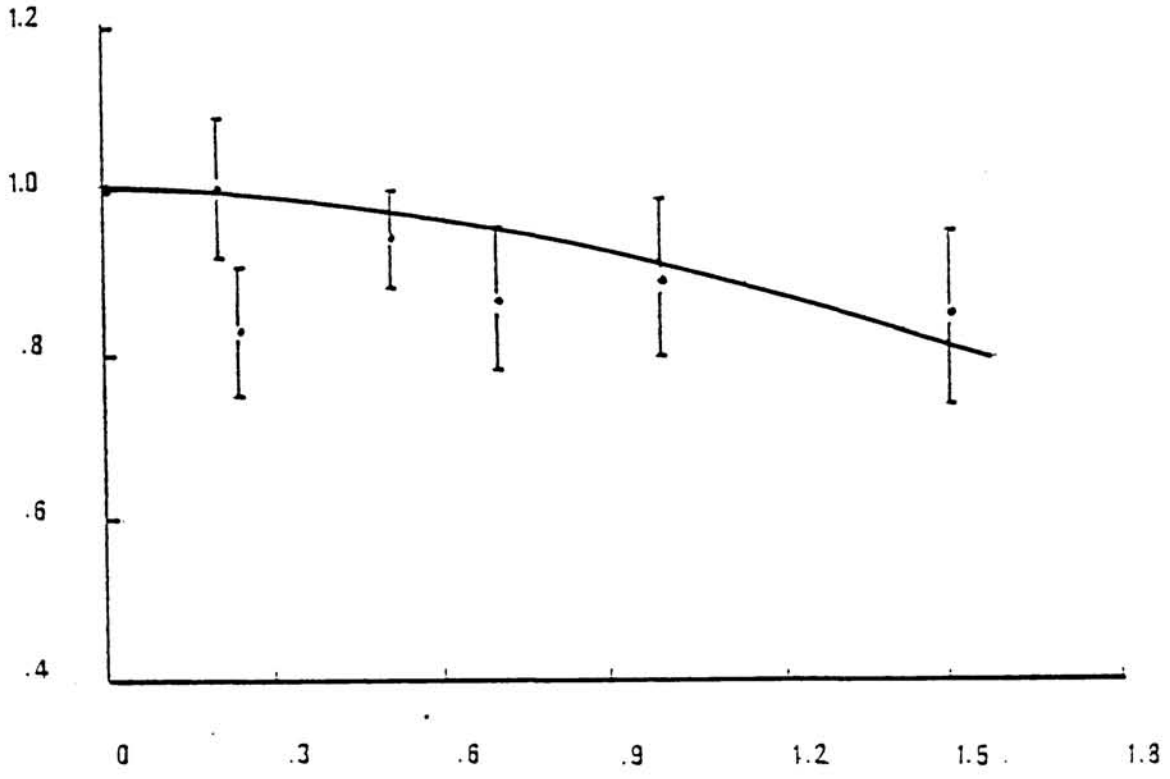
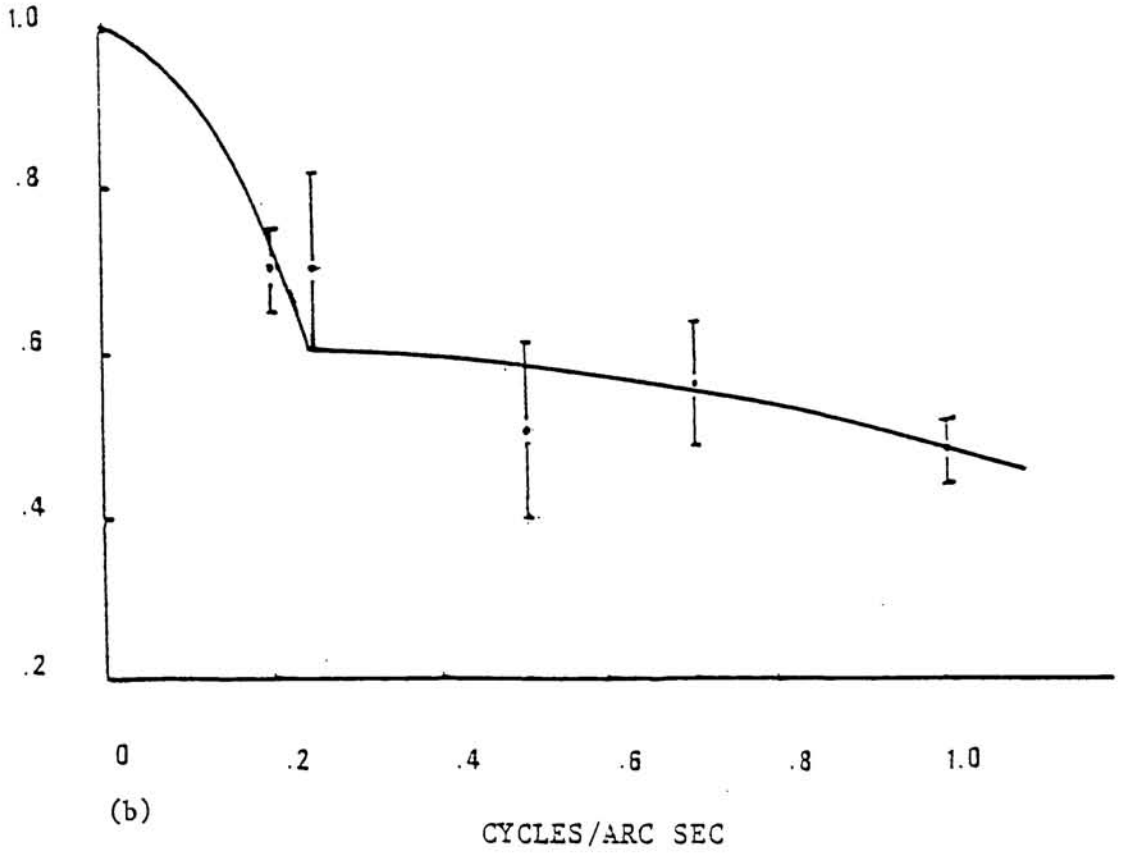


Fig.3.1 The North-South spectrum of IRC+10216

Fig.3.2 Partially recovered spectra of CIT6 (a) 3.8μm, (b) 4.8μm





in seeing and bad weather prevented enough data being obtained to determine sufficiently precise spectra recovery for CIT6 and VYCMa. For example, consider the spatial frequency power spectra of the carbon star CIT6 (Fig.3.2) at 3.8 and 4.8 microns. The error bars for spatial frequency points are large compared to the extension (unlike IRC +10216). Repeated measurements are necessary to recover the spectra accurately. The straight line curves shown for reference correspond to angular Gaussian profiles of standard deviation 0.06" at 3.8 μm, and 0.80" and 0.08" at 4.8 μm. This should be compared to corresponding Rayleigh resolutions of 0.58" and 0.82". The calibration sources used were α Boo and μ UMa.

(ii) Slit

In August 1979 the first slit measurements were taken with the system shown in Fig.2.1. Reduction of the data showed the seeing conditions to be often variable. However the 3.8 micron spectrum of GL2591 was obtained and is shown in Fig.3.3.

The spectrum of a uniform disc of extension 0.18" is plotted against the data. The source, measured in the north-south direction, is clearly unresolved.

Fig.3.4 shows the spectrum of Io: it is resolved, and is fitted by a Gaussian of width 1.6". Assuming the diameter of Io to be 3200 km, the angular diameter expected at the time of observation would be .95". As the measurement was not made with our cryostat due to a detector failure, a common user cryostat at UKIRT was substituted. This instrument had a very small bandwidth. It is difficult to say from this measurement how much detail might be measurable without this restriction but would be interesting to do for such an object, known to have a volcanic nature. A calibration error, normally evident using an instrument with sufficient bandwidth, would explain the discrepancy in the extension.

Further Developments

The main problem area for the Speckle technique is undoubtedly the turbulent nature of the atmosphere. We are currently looking for the correlation between the low frequency width and high frequency power to enable most of the data to be used.

In addition spectrum recovery requires fast transformation of the raw data. My suggestion is to digitise raw data at telescopes (other than at Tenerife) and read the data directly to magnetic tape along with

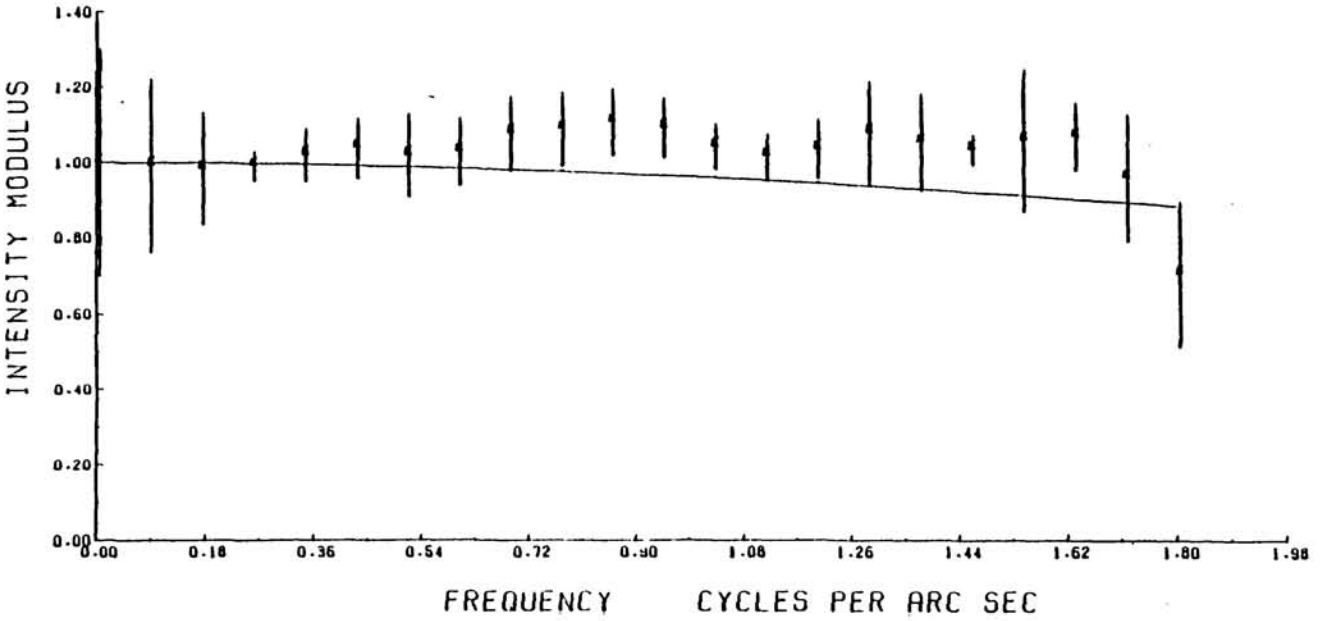


Fig.3.3 The 3.8μm spectrum of GL2891

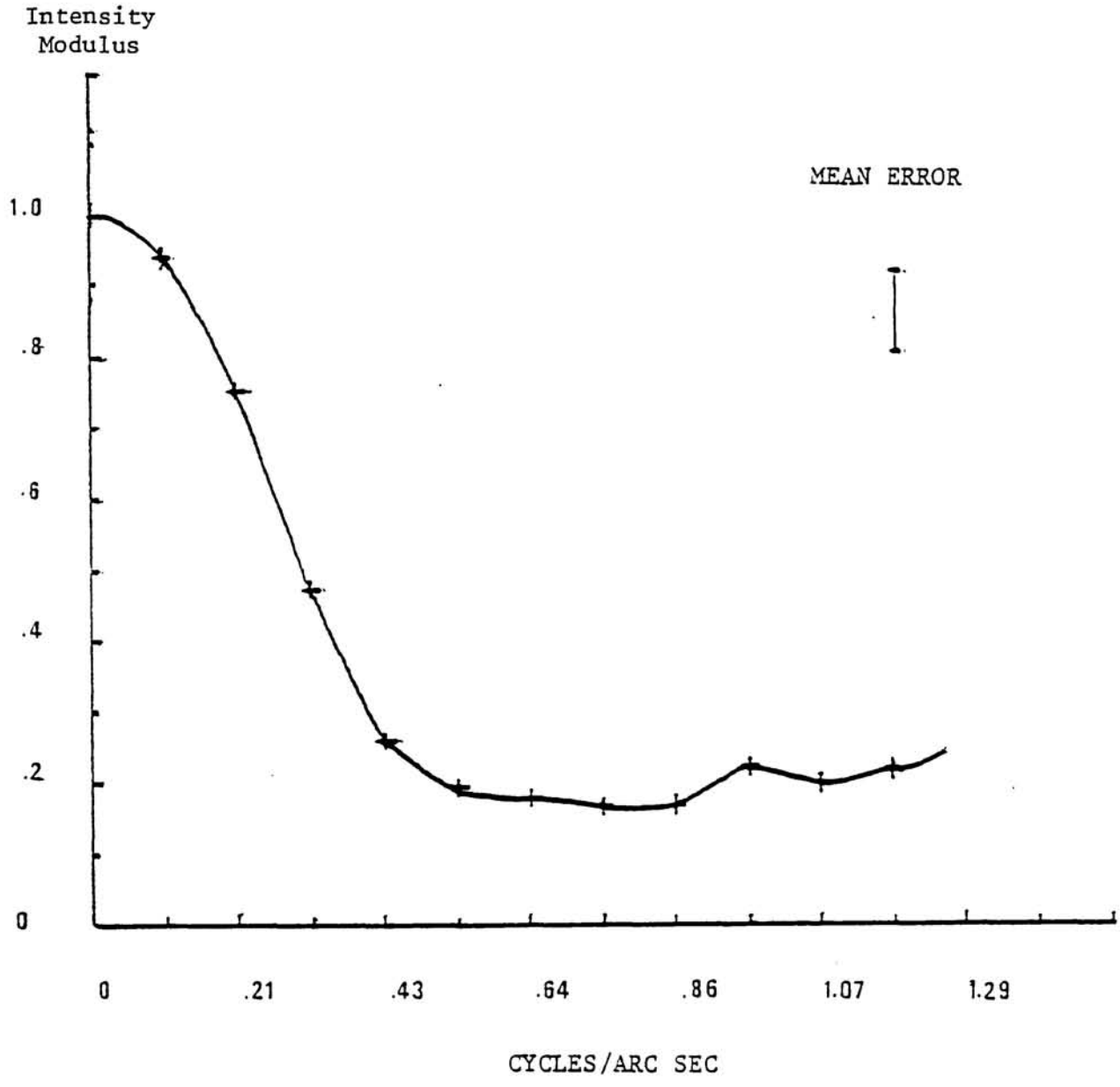


Fig.3.4 North-South spectrum of Io at 2.2μm

header (title) information. 44 Mbyte storage is available, ample for the experiment. The Astronomy Group's PDP 11/23 should be used and programmed in Fortran and assembler for

(i) automatic computation of power transforms

(ii) interactive graphical analysis to recover spectra. Fortran would allow various forms of correlation analysis to be written and tried quickly. Recovered spectra could then be transferred to the ICCC system for hard copy plotting.

With regard to the quick-look, I suggest employing a microprocessor system similar to the 4-channel common user microsystem for Tenerife which I have been developing recently. This would provide a digital quick-look having the advantage of being simpler to operate than an analogue system. However, the task is non-trivial. Processing speed and data storage demands are high to reduce the data quickly enough and for correlations to be looked for - e.g. temporal correlation and the Speckle MTF correlation already mentioned.

Above all long periods of stable seeing are required, which I have only seen in the summer months at Tenerife.

Chapter 4. The Lunar Occultation Technique

4.1 Historical Summary

Lunar occultations were one of the earliest astronomical events ever observed. However, the idea that stellar angular diameters could be measured in this way is relatively recent and due to MacMahon (1909). Whitford (1939) was the first to record an occultation photoelectrically. He showed that the diameter of the star could be deduced from the data by fitting a model which depended upon a few specific parameters.

The occultation technique, however, developed slowly. Events were rare and brief. Irregularities, such as small hillocks, at the Lunar limb caused traces to be noisy. Further degradation was caused by scintillation. Measurements required a fast recording system and lengthy analysis. The advent of the photomultiplier tube greatly increased the number of stars which were bright enough to be measured. Even so, the attempts of the early 1950's were the last for about 15 years.

Interest in the technique was raised by Edward Nather and David Evans (1970) who combined to establish the observational method and various reduction techniques. In the mid 1970's Stephen Ridgway extended the technique to infrared wavelengths with a prolific programme of observations, especially for stars of the late spectral types. There are now well over 100 measurements which represent the largest number of angular diameter measurements from a single technique.

4.2 The Occultation event

As the Moon moves between a distant star and a point on the Earth's surface it casts a shadow which moves at high speed across the ground. Closer inspection reveals the shadow not to have a sharp edge, and furthermore the light from the star consists of bright and dark fringes. If a telescope is trained on the star as this diffraction pattern passes, the light collected will fluctuate in intensity and finally drop to zero in a very short time, as the Lunar shadow becomes total. For stars with diameters of 1 to 15 m arcsec the duration of the event remains constant, but the diffraction pattern is modified (see Fig. 4.1). On more

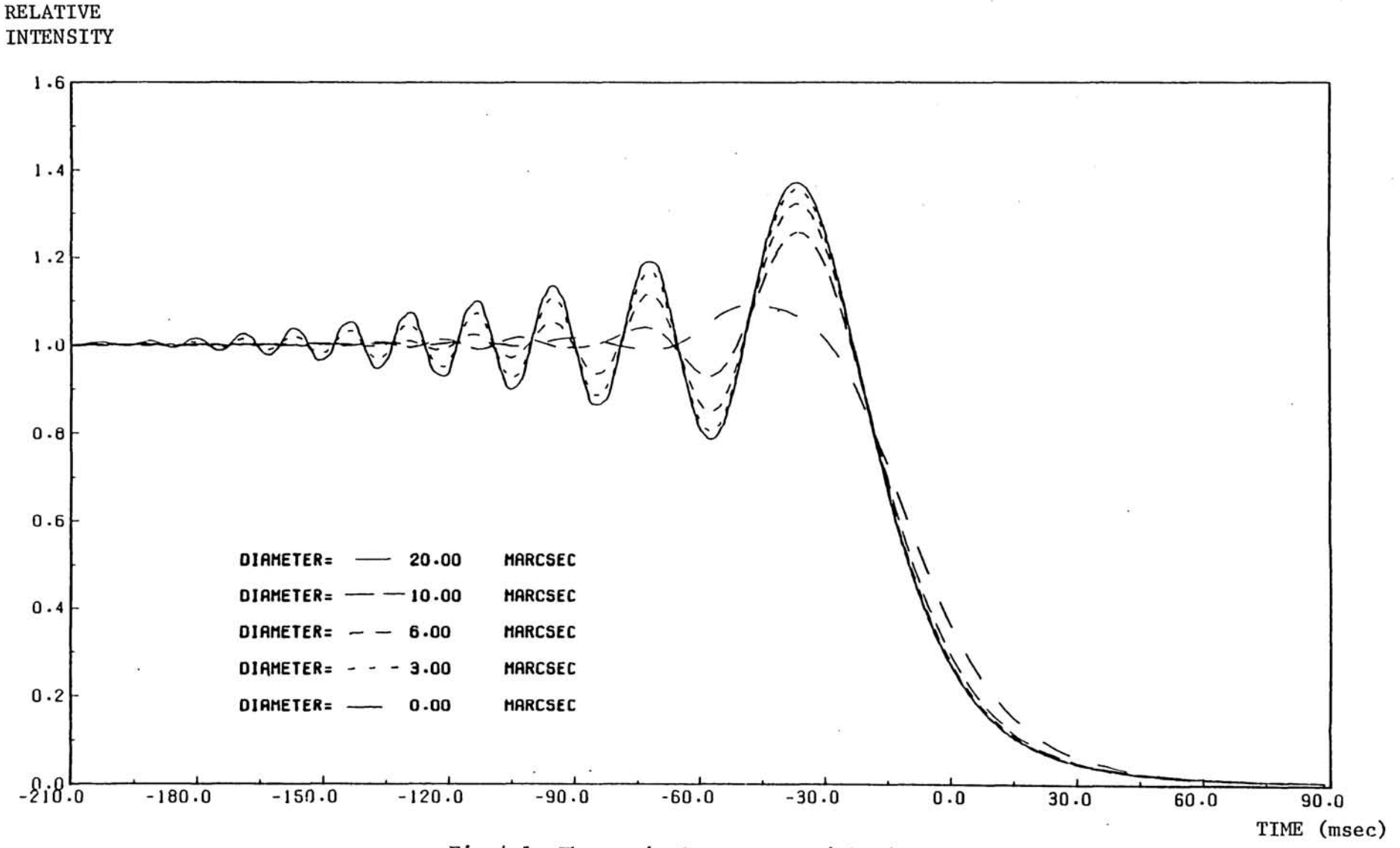


Fig.4.1 Theoretical response with diameter

extended sources diffraction effects play only a minor rôle, but the timescale is increased proportionally.

The main difficulties in the estimation of stellar diameters are:

i) Irregularities at the Lunar limb of size comparable with that of the first Fresnel zone at the wavelength of observation can cause serious distortions in the fringe pattern; smaller irregularities may produce noise. Nevertheless, following Ridgway et al (1977a), the consistency of several observations of the same source justifies the conclusion that Lunar limb effects are not a serious problem.

ii) Scintillation, which is important at large zenithal distances, can disturb the fringe pattern and so degrade the results.

4.2.1 The reduction model

The intensity pattern expected when a monochromatic point source is obscured by a straight edge can be described in terms of classical Fresnel integrals:

$$c(\omega) = \int_0^{\omega} \cos(\tfrac{\pi}{2}\tau^2)\,d\tau \text{ and } s(\omega) = \int_0^{\omega} \sin(\tfrac{\pi}{2}\tau^2)\,d\tau \qquad (4.1)$$

(Born and Wolf, 1975)

If y is the linear distance orthogonal to the occulting edge and d the distance to the Moon, the intensity is

$$f(y,\lambda) = \tfrac{1}{2}\left((c(\omega)+\tfrac{1}{2})^2 + (s(\omega)+\tfrac{1}{2})^2\right) \qquad (4.2)$$

where ω is the dimensionless Fresnel argument

$$y\sqrt{\frac{2}{\lambda d}}$$

The observed intensity distribution is a function of the extended source distribution, the extended aperture of the telescope and the optical and electrical bandwidth. The optical bandwidth forms a multiplication and the remaining factors produce convolutions with the monochromatic point source function.

I define:

i) $s(\lambda)$: the sensitivity of the equipment and the intensity

distribution of the star which is normalised integrally.

$$\int_0^\infty s(\lambda)d\lambda = 1 \qquad (4.3)$$

The sensitivity function is the product of the sky filter profile and the spectral intensity distribution. I assume the latter to be a blackbody function as measured by a detector with a sensitivity which is inversely proportional to wavelength:

$$s(\lambda) \propto F(\lambda)B(\lambda)$$

and
$$B(\lambda) \propto \frac{\lambda^{-4}}{\exp(\frac{hc}{\lambda kT} - 1)} \qquad (4.4)$$

ii) $\phi(y)$ the aperture weighting function

$$\phi(y) = A\{(1-(y/R1)^2)^{\frac{1}{2}} - (R2/R1)(1-(y/R2)^2)^{\frac{1}{2}}\} \quad -R2<y<R2$$
$$\phi(y) = A\,(1-(y/R1)^2)^{\frac{1}{2}} \quad -R1<y<-R2,\ R2<y<R1 \qquad (4.5)$$
$$\phi(y) = 0 \quad \text{otherwise.}$$

A is a normalisation constant, $A = 1/\int_{-\infty}^{\infty}(y)dy$
R1 is the radius of the primary
R2 is the radius of the central obscuration.

iii) $\psi(\alpha,\beta,R)$: the source function (see Diercks and Hunger, 1952)

$$\psi(\alpha,\beta,R) = \frac{\frac{2}{\pi}(1-(\frac{\alpha}{R})^2)^{\frac{1}{2}} + \frac{1}{2}\beta(1-(\frac{\alpha}{R})^2)}{(1+2/3\beta)R} \quad -R<\alpha<R \qquad (4.6)$$

$$0 \quad \text{otherwise}$$

α is an angular variable and equals y/d radians
β is the limb darkening coefficient
R is the angular radius of the star (radians).

If at this stage I neglect the effect of the electrical system, the expression for the observed fringe pattern is

$$F = E_o + i_o \int_o^\infty s(\lambda) f(y,\lambda) * \phi(y) * \psi(y/d,\beta,R) d\lambda \qquad (4.7)$$

E_o and i_o are respectively the background level and the intensity of the star.

With an integrating system, the expression for each point of the curve is

$$F_j = E_o + i_o \int_{v(t_j-\tau_o)}^{v(t_{j+1}-\tau_o)} \int_o^\infty s(\lambda)\, f(y,\lambda) * \phi(y) * \psi(y/d,B,R) dy d\lambda. \qquad (4.8)$$

where v is the velocity of the fringe pattern and τ_o the time of geometric occultation of the stellar centre.

4.2.2 The stochastic model

Sections 4.2.2 and 4.2.3 follow the work of Knoechel and Heide (1978). Five basic parameters are adjusted:

p1=E_o, sky background = Y displacement
p2=i_o, star intensity = Y magnification
p3=τ_o, occultation time = X displacement
p4=v velocity of moon = X magnification
p5=R radius of the star

a) The adjustment is performed by a least squares fitting procedure. If p(k) are the unknowns computed by the (k-1) iteration step, $\Delta p(k)$ are found by solving the equations

$$A_{(k)}\, \Delta p_{(k)} = \Delta u_{(k)} \qquad (4.9)$$

where $A_{(k)ji} = (\partial F_j / \partial p_i)_{p=p(k)}$

and $\Delta u_{(k)j} = E_j - (F_j)_{p=p(k)}$

The number of equations is reduced by multiplying both sides of Equ.4.9 by $A^\tau_{(k)}\, C^{-1}_{(k)}$

$$A^\tau_{(k)}\, C^{-1}_{(k)} A_{(k)} \Delta p_{(k)} = A^\tau_{(k)} C^{-1}_{(k)} \Delta u_{(k)} \qquad (4.10)$$

where τ denotes transposition and C is the covariance matrix of the measurements E_j. The elements of C are

$$C_{jj} = F_j,\ C_{ij} = 0 \tag{4.11}$$

The partial derivatives A_{ji} are given by

$$A_{j1} = 1$$

$$A_{j2} = (F_j - E_o)/i_o$$

$$A_{j3} = -v\ (I(x_{j+1}) - I(x_j))$$

$$A_{j4} = (t_{j+1} - \tau_o)I(x_{j+1}) - (t_j - \tau_o)I(x_j) \tag{4.12}$$

$$A_{j5} = i_o \int_{x_j}^{x_{j+1}} \int_o^\infty s(\lambda) f(y,\lambda) * \phi(y) * \partial\psi/\partial R(y/d, \beta, R)\, dy d\lambda$$

$$I(x) = i_o \int_o^\infty s(\lambda) f(y,\lambda) * \phi(y) * \psi(y/d, \beta, R)\, d\lambda .$$

$$x_j = v(t_j - \tau_o)$$

$$\partial\psi/\partial R = \frac{\alpha^2/R^4 . \frac{2}{\pi}(1-(\alpha/R)^2)^{-\frac{1}{2}} + \beta}{1+2/3.\beta} - \frac{2/\pi(1-(\alpha/R)^2)^{\frac{1}{2}} + \frac{1}{2}\beta(1-(\alpha/R)^2)}{(1+2/3.\beta)R^2} \tag{4.13}$$

b) The reduced chi-square is defined by

$$m = \Delta u_{(k)}^{\tau} C_k^{-1} \Delta u_{(k)} / (N-5)$$

where N is the number of points.

$$m = (N-5)^{-1} \sum_{j=1}^{N} (E_j - F_j)^2 / F_j$$

When E_j is dimensionless (expressed in the number of photons) the reduced chi-squared is unity if the adjustment is not questionable.

c) Another advantage of multiplying Equ.4.9 by $A^{\tau}_{(k)}C^{-1}_{(k)}$ is that the standard deviations of the computed unknowns are the square root of the diagonal elements of $(A^{\tau}_{(k)}C^{-1}_{(k)}A_{(k)})^{-1}$. If E_j is not expressed in number of photons, the standard deviations computed for the unknowns p_i have the dimensions $p/\sqrt{E}$. I have therefore adopted the procedure used by Ridgway to make them dimensionless. That is, I multiply the standard deviations by the square root of the chi-square. There is another advantage; if the adjustment is not questionable, the standard deviations computed by this method will be the same as the ones computed if the signal was dimensionless; if the adjustment is questionable, the dimensionless reduced chi-squared is much larger than unity and the standard deviations are increased.

4.2.3 Lunar Occultations disturbed by Scintillation

The measured occultation pattern is the Fresnel curve disturbed by atmospheric scintillation. There are two statistically rigorous methods for the reduction of such observations. Scintillation

i) introduces correlation to successive data points by modifying the covariance matrix of the measurements

ii) may be represented by polynomials weighted according to the scintillation power spectrum.

These methods plus the least squares procedure are applied by Knoechel and Heide (1973) to a large number of simulated Lunar occultation measurements. They show that angular diameters from the classical method can be statistically incorrect, especially for zenithal distances beyond 40^{o}.

As the polynomial method is a natural extension of the classical model, I have applied it to take account of scintillation.

The scintillation is introduced as a disturbing function H(y) into the theoretical expression for each point of the curve.

$$F_i^{*}=E_o+i_o\int_{V(t_i-\tau_o)}^{V(t_{i+1}-\tau_o)}\int_{o}^{\infty}(1+H(y)).s(\lambda).f(y,\lambda)*\phi(y)*\psi(\frac{y}{d},\beta,R)\,dy\,d\lambda. \qquad (4.14)$$

H is written as a series of Legendre-polynomials L_i

$$H(y)=\sum_{i=1}^{m} q_i.L_i\left(\frac{y+V\tau_o}{y_N+V\tau_o}\right);\quad -V\tau_o\leq y\leq y_N \tag{4.15}$$

The q_i are additional unknowns of the adjustment; initial values are zero.

With the same notation as in the last section

$$I(x)=i_o\int_o^{\infty}(1+H(y)).s(\lambda).f(y,\lambda)*\phi(y)*\psi(\frac{y}{d},\beta,R)\,dyd\lambda. \tag{4.16}$$

$$A_{j5}=i_o\int_{x_j}^{x_{j+1}}\int_o^{\infty} L_i(u).s(\lambda).f(y,\lambda)*\phi(y)*\psi(\frac{y}{d},\beta,R)\,dyd\lambda;\ \text{with } u=\frac{y+V\tau_o}{y_N+V\tau_o} \tag{4.17}$$

In fact the q_i are totally free and the expression H would suffice to fit the occultation curve; for the process to be correct we have to include some additional equations. The additional partial derivatives needed for the reduction are

$$A_{N+i,l}=\begin{cases}1 & \text{for } l=i+5,\ i=1,\ldots,m\ \ l=1,\ldots,5+m\\ 0 & \text{otherwise}\end{cases} \tag{4.18}$$

and the covariance matrix becomes

$$C_{ii}=\begin{cases}F_i & \text{for } i=1,\ \ldots,\ N\\ a_k & \text{for } i=N+k\end{cases}\qquad C_{ij}=0 \text{ for } i\neq j \tag{4.19}$$

where the coefficients a_k are the standard deviations of the coefficients q_i. I assume they are the same in the visible as in the near infrared. The coefficients a_k are given in table 4.1 for different zenithal distances.

Table 4.1

k	Z=26°	Z=49°	Z=58°	Z=69°
I	0.017	0.054	0.095	0.109
2	0.017	0.048	0.084	0.099
3	0.014	0.042	0.065	0.110
4	0.012	0.036	0.051	0.113
5	0.010	0.029	0.043	0.100
6	0.009	0.024	0.036	0.083
7	0.012	0.023	0.034	0.070
8	0.014	0.023	0.030	0.062
9	0.013	0.023	0.028	0.058
10	0.010	0.021	0.026	0.056
11	0.008	0.019	0.024	0.056
12	0.005	0.016	0.022	0.052
13	0.007	0.014	0.023	0.046
14	0.004	0.014	0.025	0.040
15	0.002	0.015	0.023	0.036
16		0.015	0.020	0.037
17		0.016	0.024	0.039
18		0.015	0.021	0.036
19		0.014	0.018	0.035
20		0.014	0.020	0.036
21				0.029
22				0.027
23				0.033
24				0.025

Standard deviations of the coefficients q_i of the Legendre-polynomials L_i at different zenithal distances Z.

4.2.4 Electrical deconvolution

The Fresnel pattern originating at the Lunar limb is swept across the observation point on the ground at high speed. The intensity variation is therefore modified by the transfer function of the detection electrical system. As this transfer function can be measured accurately, its convoluting effect can be removed before model fitting.

If o(t) is the measured occultation and f(t) the electrically deconvolved Fresnel curve, then

$$o(t) = f(t)*i(t) \qquad (4.20)$$

where i(t) is the system impulse response and * denotes convolution. In the Fourier plane

$$F(f) = \frac{O(f)}{I(f)} \tag{4.21}$$

where O(f), I(f) and F(f) are the complex Fourier transforms of o(t), i(t) and f(t). The real and imaginary parts of F(f) are therefore

$$\begin{aligned} F_R(f) &= (O_R(f)I_R(f)+O_I(f)I_I(f))/A \\ F_I(f) &= (O_I(f)I_R(f)-O_R(f)I_I(f))/A \end{aligned} \tag{4.22}$$

and $$A = I_R^2(f) + I_I^2(f)$$

The inverse Fourier transform of F(f) is

$$f(t) = ICT\ (F_R(f)) + (IST\ \ F_I(f)) \tag{4.23}$$

where and $\begin{matrix} ICT \\ IST \end{matrix}$ represents inverse $\begin{matrix} cosine \\ sine \end{matrix}$ transform.

I decided to band limit f(t) to 250Hz below which all information about the stellar diameter lies. The sample period was increased to 2 msec to reduce the computation time in the subsequent modelling.

4.3 General Observational and Signal to Noise Considerations

Ridgway (1977b) gives estimates of the various observational parameters and signal to noise constraints. Tbl.4.2 shows the limiting angular resolution for the various convolutions and in addition two approximations are referred to: the Geometrical, when there are only minor diffraction effects, and the Fresnel, when several fringes are visible.

The cases of source photon, detector and background photon noise limited performances are considered. For each, the minimum diameter measurable (θ_m) is calculated for the Fresnel and Geometrical approximations. For the former, both the electrical bandwidth

$$f_m = V/d\theta_m \qquad (4.24)$$

(V is the orbital speed)

and the optical bandwidth

$$\Delta\lambda = d\theta_m^2 \qquad (4.25)$$

(D is the primary diameter)
d is the Earth-Moon distance.

are constrained. Only Equ.4.24 applies in the geometrical case.

Ridgway approximates the detected flux by

$$F_o = \alpha F(\lambda)\Delta\lambda\frac{\pi D^2}{4} \text{ Watts} \qquad (4.26)$$

where $F(\lambda)$ is the flux ($Wm^{-2}\mu m^{-1}$)

and α is the quantum efficiency.

Table 4.2

Electrical bandwidth	$447/f_m$(Hz)
Telescope diameter	1.1 D(m)
Optical bandwidth	10.1 $\sqrt{\Delta\lambda}$(μm)
Fresnel limit	$< 3.7\sqrt{\lambda}$(μm)
Geometric limit	$> 9.8\sqrt{\lambda}$(μm)

Basic constraints for ground based observations of lunar occultations (see text)

(1) Source photon noise limited detection

The detected flux is

$$n(\lambda) = \frac{\lambda}{hc} F_o \text{ photons } s^{-1} \qquad (4.27)$$

and with electrical bandwidth f_m(Hz), the photon signal to noise ratio is

$$S_n = \sqrt{\frac{n(\lambda)}{f_m}} \tag{4.28}$$

Combining Equ.4.26, Equ.4.27 and Equ.4.28

$$S_n^2 = \left(\frac{\lambda}{hc}\alpha F(\lambda)\Delta\lambda\frac{\pi D^2}{4}\frac{1}{f_m}\right)^{\frac{1}{2}} \tag{4.29}$$

(i) Geometric limit

Equ.4.24 and Equ.4.29 solved for θ_m gives

$$\theta_m = \frac{S_n^2 V}{\frac{\lambda}{hc}\alpha F(\lambda)\frac{\pi D^2}{4}\Delta\lambda d} \tag{4.30}$$

(ii) Fresnel limit

Introducing Equ.4.25 into Equ.4.30 gives

$$\theta_m = \left[\frac{S_n^2 V}{\frac{\lambda}{hc}\alpha F(\lambda)\frac{\pi D^2}{4}d^2}\right]^{1/3} \tag{4.31}$$

(2) Detector noise limited detection

The signal to noise in this case is

$$S_n = \frac{F_o}{B\sqrt{f_m}} \tag{4.32}$$

where B is Noise Equivalent Power per $\sqrt{}$(unit frequency).

(i) Geometric limit

Substituting Equ.4.24 and Equ.4.26 into Equ.4.32

$$\theta_m = \frac{S_n^2 B^2 V}{\left(aF(\lambda)\frac{\pi D^2}{4}\right)^2 d} \tag{4.33}$$

(ii) Fresnel limit

Again, using Equ.4.25 and Equ.4.33

$$\theta_m = \left[\frac{S_n B}{\alpha F(\lambda)\frac{\pi D^2}{4}}\right]^{2/5} \left[\frac{V}{d^3}\right]^{1/5} \qquad (4.34)$$

(3) Background photon noise limited detection

The background flux may be represented by $\beta D^2 \Delta\lambda$ where the significance of β depends on the specific observational situation. In this case

$$S_n = \frac{n(\lambda)}{\sqrt{\beta D^2 \Delta\lambda f_m}} \qquad (4.35)$$

(i) Geometric limit

Equ.4.24, Equ.4.26 and Equ.4.35 combine to give

$$\theta_m = \frac{S_n^2 \beta V}{\left[\frac{\lambda}{hc}\alpha F(\lambda)\frac{\pi}{4}\right]^2 d\Delta\lambda} \qquad (4.36)$$

and finally

(ii) Fresnel limit gives

$$\theta_m = \left[\frac{S_n}{\frac{\lambda}{hc} F(\lambda)\frac{\pi dD}{4}}\right]^{2/3} (\beta V)^{1/3} \qquad (4.37).$$

Ridgway uses 4.26 to 4.37 to estimate the performance of the occultation technique at 0.55(V), 2.2(K) and 10.6(N) microns. It is immediately noticable that even for apertures greater than 1m, only small regions of the angular diameter-V/K/N diagrams are unavailable. The decrease in atmospheric scintillation with increasing aperture and higher limiting magnitude clearly justifies the application of large telescopes for occultation work.

Chapter 5. Techniques and Instrumentation

5.1 The Observational method

Near infrared Lunar Occultations have been measured over the past two years with the 1.5m flux collector at Tenerife. The telescope, photometer cage and detector cryostat have already been described in section 2.4.

The Royal Greenwich Observatory has provided us with annual predictions of Lunar occultations since January 1978. The sources were

(i) Visible stars brighter than V = 7.5.

(ii) Stars from the two micron survey.

The most favourable observations were disappearances in the first quarter of each Lunar month. At this time there is little radiation reflected by the Moon and scattered by the Earth's atmosphere. Furthermore, Earthshine reveals the Lunar limb. To observe a reappearance is more difficult. The telescope must be capable of accurate absolute pointing or offsetting to within 10 arcsec. I have not yet managed to measure a reappearance with this telescope.

Finders were prepared from the Smithsonian Astrophysical Observatory (SAO) star charts. This involved noting the positions of several conveniently placed bright stars for offsetting purposes. Sources were located thirty minutes before events.

The optical filter chosen depended upon the magnitude of the source and the sensitivity of the detector system. Usually a narrow bandwidth filter $\Delta\lambda$ = 0.04 microns was used for maximum angular resolution. However if the source had a large enough blackbody diameter, a larger bandwidth would be selected to improve the signal to noise ratio. The focal plane aperture ($10''$) was a compromise between increasing background radiation and tolerance to guiding errors. The DC amplifier gain was set to give a $\frac{1}{2}$ volt signal change on and off the source. The amplifier bandwidth was selected and a permanent record of the DC signal taken on a pen chart recorder. Tape recording was started a few minutes before the occultation was due.

5.2 Signal Processing and Data Acquisiton

It is difficult to maintain the visibility of the fringes during an occultation. For bright sources measurements with the low feedback resistance do not limit the angular resolution. For weaker sources the high load resistance was needed and used along with the roll up amplifier described in section 2.4.1 (see fig.5.1).

Recording an occultation is a choice between digital and analogue methods. The former is not accomplished until the data is transferred to a permanent storage medium but is more straightforward. The latter has a signal to noise ratio limited by tape noise, but is safer.

I have digitised analogue recordings in the laboratory. An assembler programme sampled the Fresnel patterns at 2K samples per sec, which avoided aliasing the signal. Half a page (128 bytes) of memory was repeatedly displayed on a VDU to establish where the event was located. The data was then transferred under programme control via a V24 interface (electronics link) to a PDP 11/23. I then stored the data on paper tape and disc. Another programme passed the data to the ICCC mainframe across another V24 interface for deconvolution and modelling. The system has been developed to provide a quick efficient method for making available the raw data to the mainframe for reduction.

In section 4.2.4. I said that the transfer function of the detection electrical system could be measured accurately. I have developed a way of doing this. The AIM 65 microprocessor provided 50 microsecond pulses to drive an IR LED. The pulses were detected, amplified and tape recorded, along with trigger pulses. These were recovered on play back, to mark the beginning of the system impulse responses which were amplified and digitised at 2K samples per second. Several hundred pulses were used to estimate the mean response. Individual data points were accurate to 1%.

The mean impulse response was computed in the laboratory and transferred in the same way as the occultation data.

5.3 Occultation Reduction Files

The electrical deconvolution, classical and scintillation model fitting programmes had the following file arrangements:

1 Main programme (FORTRAN IV)

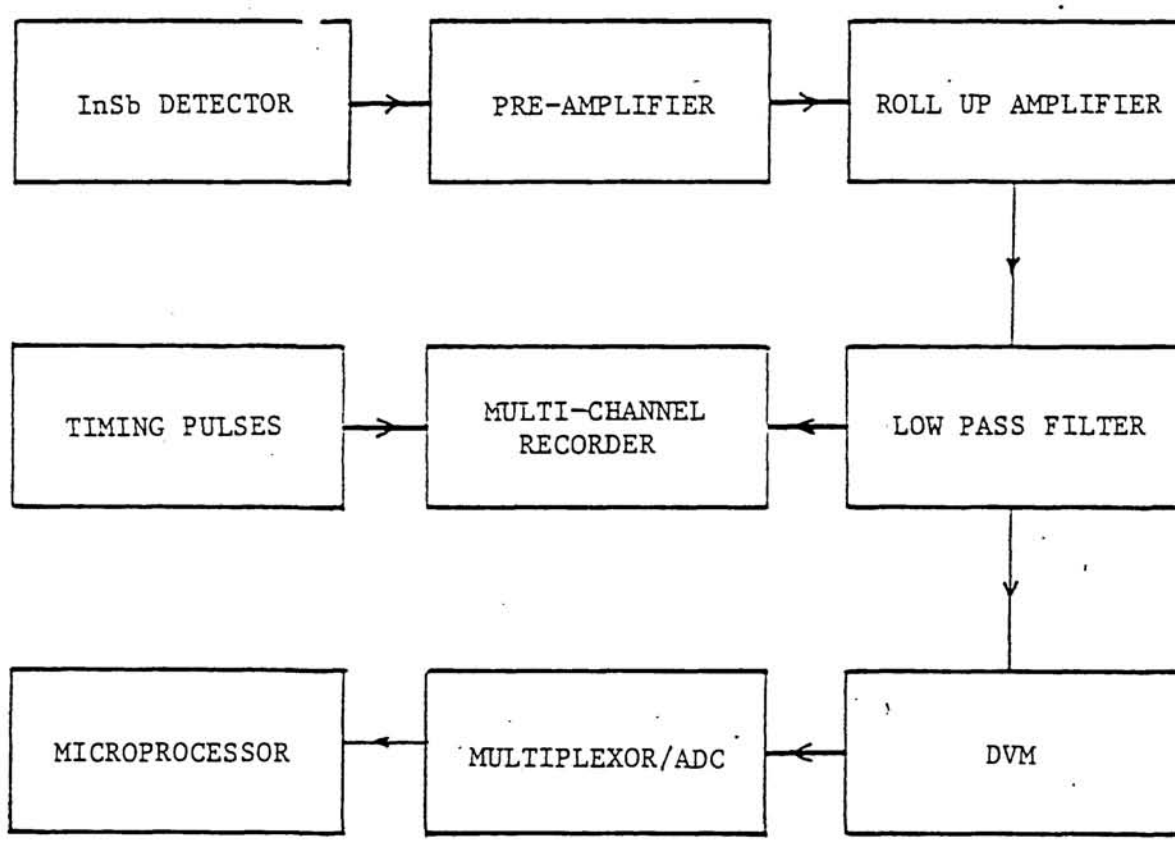


Fig.5.1 Lunar Occultation data acquisition system (includes absolute timing of the event)

2 Parameter

3 Procedure

4 Result

The main programme statements are unaltered each time new data is reduced. However the dimensions of most arrays do change with the number of data points in the model fitting programmes. The file names for the three programmes are given in Tbl.5.1.

Table 5.1

	Electrical Deconvol^{n}	Classical Reduction	Reduction with Scintill^{n}
Main	EDEC	ORE	ORES
Compiled	CEDEC	CORE	CORES
Parameter	PEDEC	PORE	PORES
Procedure	PREDEC	PRORE	PRORES
Result			

Occultation reduction files

Chapter 6 Occultation Results

6.1 Computational tests and limiting resolution

The classical model angular diameter temperature, limb darkening and sample length have been studied on the source IRC -20747, occulted on the 4th September 1979.

i) Temperature

The angular diameter was found to be insensitive to the blackbody temperature, which was varied from 3500 to 10000K. The total reduction in angular diameter corresponded to only 0.1% of the adopted value, taken at T = 5000K.

ii) Limb darkening

The limb darkening coefficient was varied from $\beta = 0$ to $\beta = 1$ and gave a value of 1.05 for the ratio of the fully darkened to uniform disc. This value may vary from event to event.

iii) Data length

Knoechel and Heide (1978) argue that the diameters computed using the classical method are strongly dependent on the length of the data sequence. I found this not to be true when little scintillation is present. Furthermore, there were only slight differences in the occultation time, Lunar velocity and diameter, consistent within the error limits. When diffraction effects dominate the precision on the occultation time and the velocity of the Moon are better than 1 msec and 1 cm/msec. On large diameters when diffraction effects are smaller, the uncertainty on these parameters will be larger due to a possible Lunar slope, leading to a large uncertainty in the diameter.

iv) Limiting resolution

The resolution is mainly limited by the optical bandwidth and the telescope aperture. Applying the relevant formulae from Tbl.4.2, for a 1.5m telescope and a 0.2 micron optical bandwidth:

$$\phi_{0.2 \text{ micron}} = 4.8 \text{ msec} \quad \text{and} \quad \phi_{1.5m} = 1.65 \text{ msec}$$

Ridgway's calculations were conservative, based upon the assumption that the information on the diameter was contained in the last detectable fringe. However most of the useful information lies in the amplitude of

fringes 2-3 times lower in frequency. This leads to:

$$\phi_{0.2 \text{ micron}} \simeq 2.4 \text{ msec}, \quad \phi_{1.5m} \simeq 0.8 \text{ msec}.$$

I have applied a more accurate method to determine the limiting resolution. The procedure, which follows the work of Nather and McCants (1970), was to generate a series of point source curves, each modified by the effects of a different optical bandwidth, gaussian in shape and centred on 2.2μm. The effective bandwidth was taken to be the full width at half-maximum. These curves were then provided as input to the program, but with the restriction that they were to be considered monochromatic. The program was then constrained to regard any modification of the basic pattern as being due to a source of finite diameter, and thus to define the size of the "spurious disk" represented by a particular bandpass selected. Figure 6.1 shows the resolution as a function of the bandwidth with $\phi_{\Delta\lambda} = 7.4\ (\Delta\lambda)^{\frac{1}{2}}$. The aperture effect is considered in the same way and in this case the limiting resolution was equal to the size of the aperture as seen from the Moon; this led to $\phi_d(\text{ms}) = 0.54\ d$. With these criteria I found

$$\phi_{0.2\ \mu m} = 3.3 \text{ ms of arc and } \phi_{1.5m} = 0.81 \text{ ms of arc}$$

values which are in good agreement with the resolution obtained by applying the corrected formulae of Ridgway.

I have applied the same method with the experimental filter first used (width = 0.2μm) and found

$$\phi_{exp} = 3.14 \pm 0.06 \text{ ms of arc.}$$

6.2 The electrical system response

Fig.6.2 shows the sampled mean impulse responses and Fig.6.3 the corresponding power transformations, for three cases

(a) $R_L = 10^8\ \Omega$

(b) $R_L = 10^{10}\Omega$

(c) $R_L = 10^{10}\Omega$ plus roll up amplification.

(R_L represents the feedback resistance of the preamplifier.) As indicated in section 5.2, the responses were induced from a pulsed IR LED.

The system corresponding to case (b) has not been used for observations. Deconvolution trials with this response degraded the

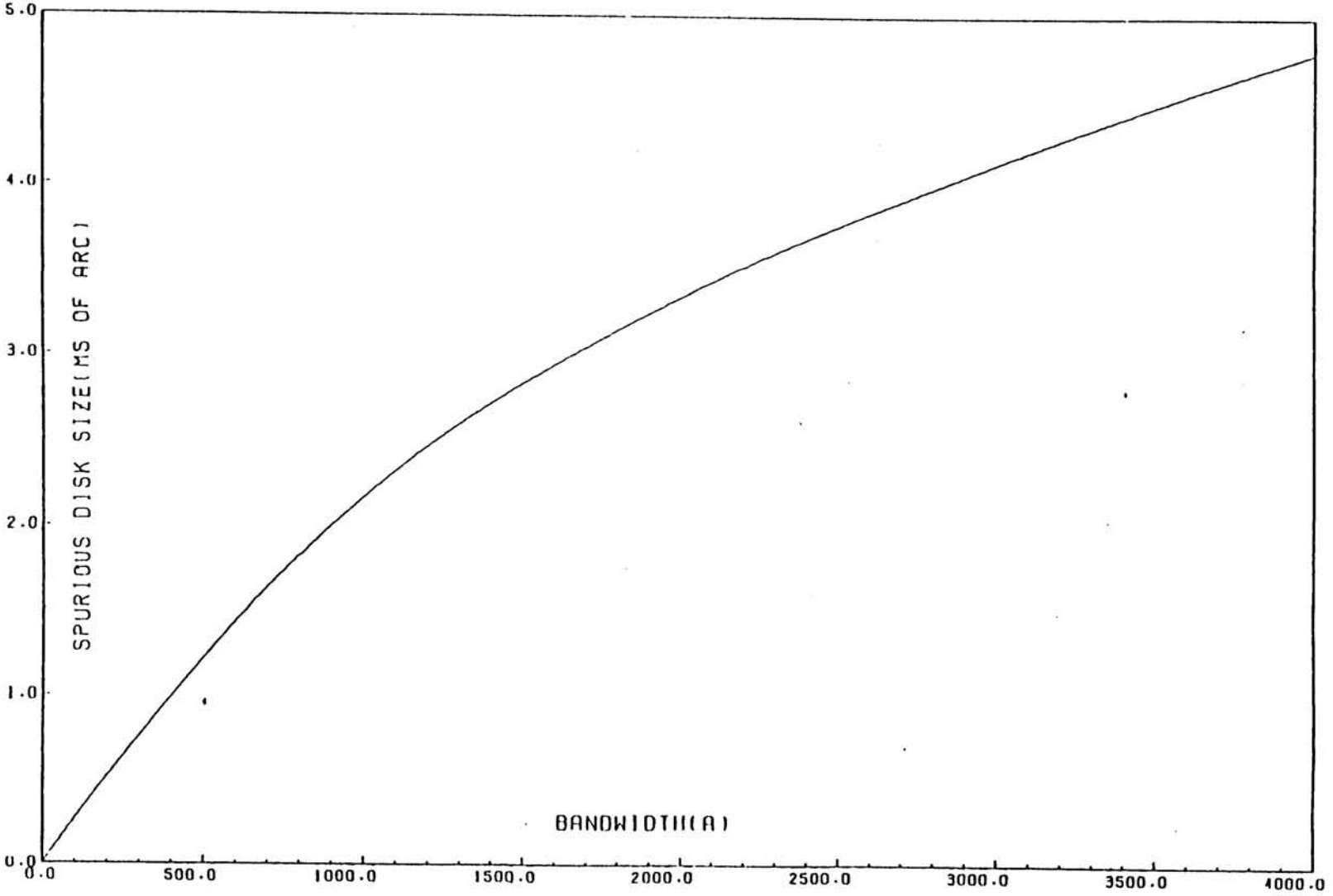
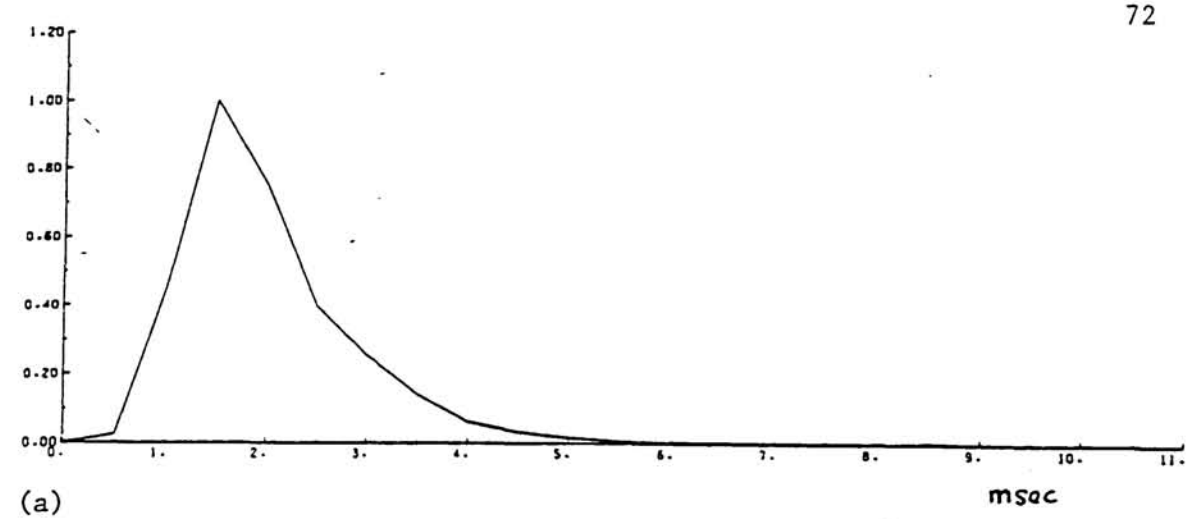
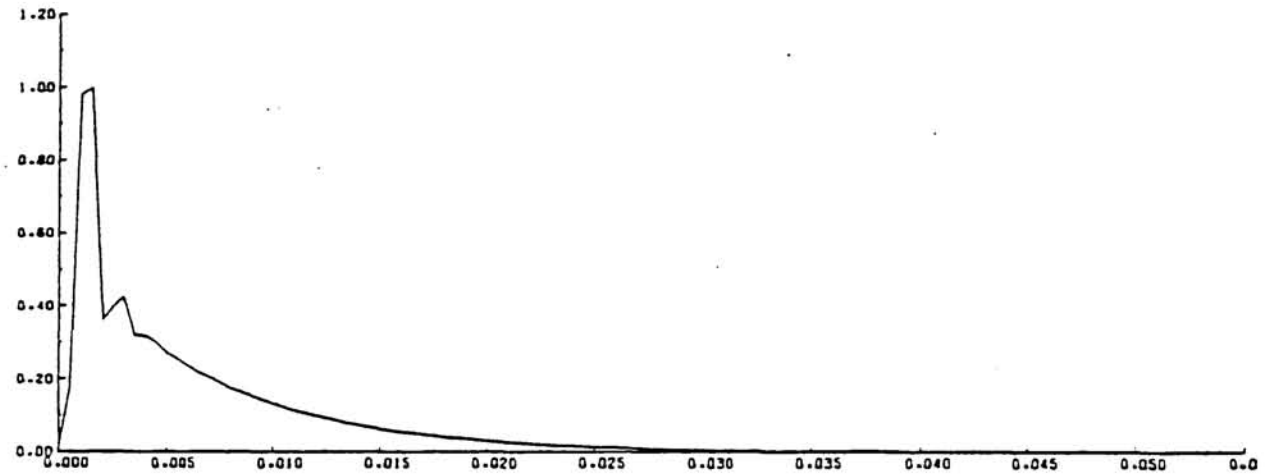


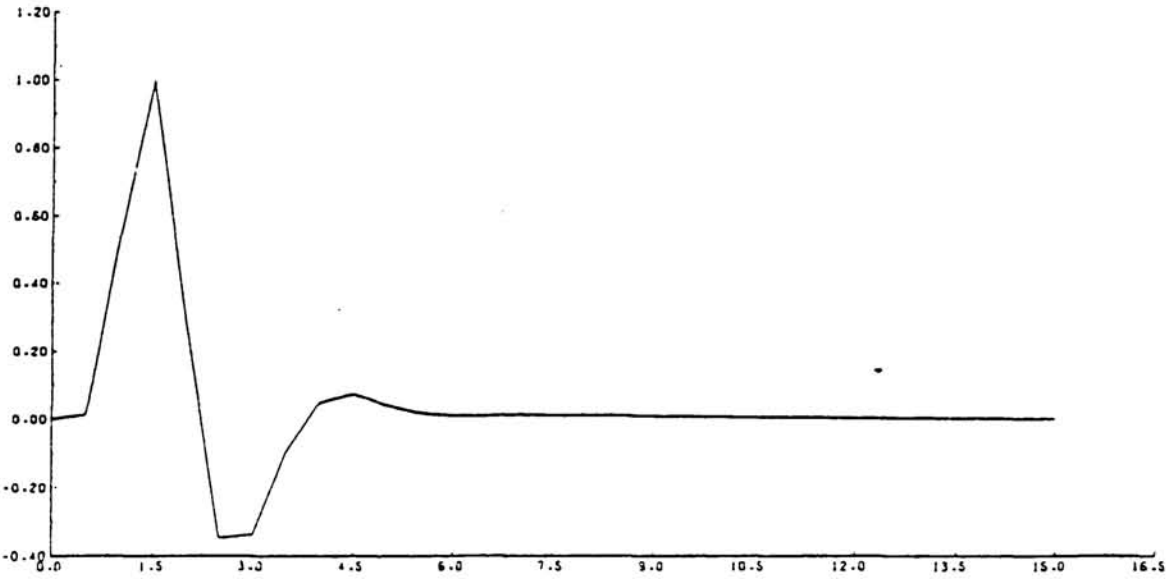
Fig.6.1 Angular resolution as a function of optical bandwidth



(a)

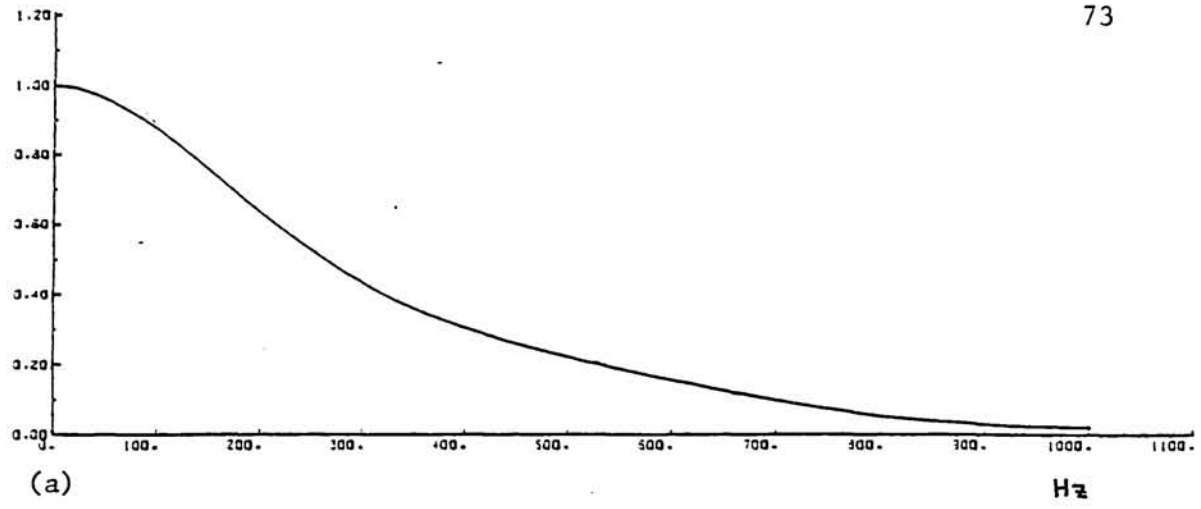


(b)

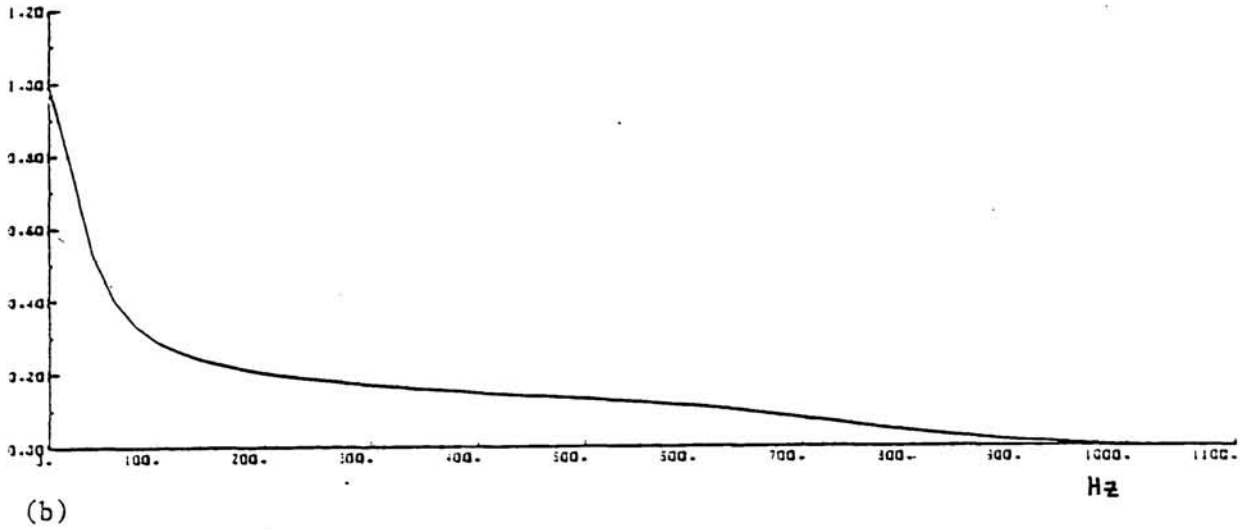


(c)

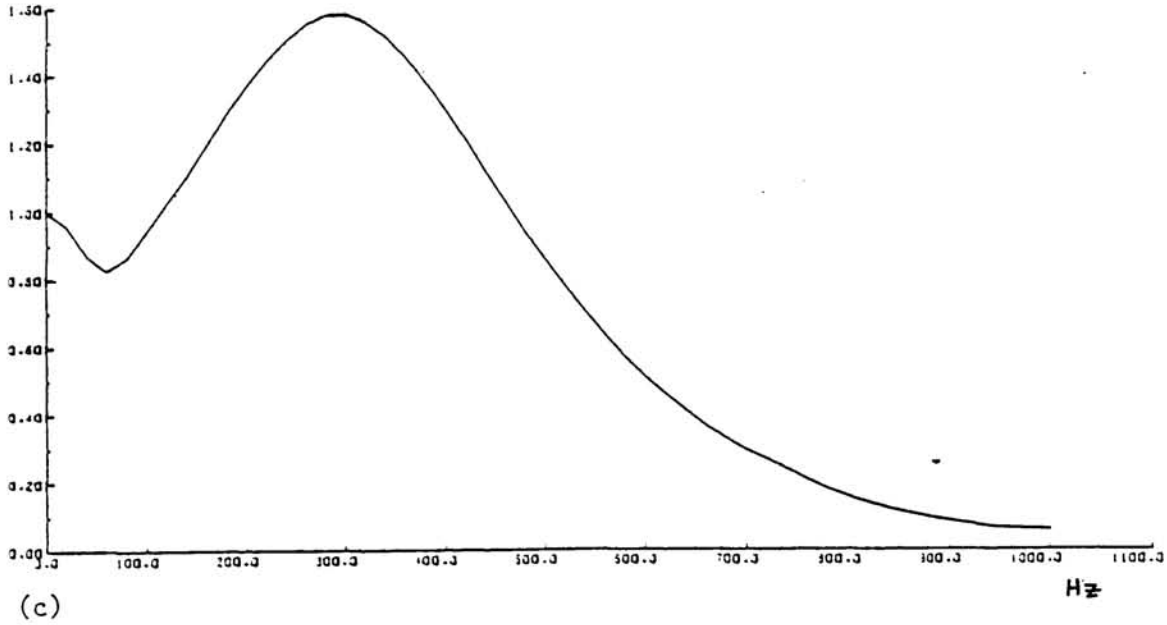
Fig.6.2 Mean digitised impulse responses (see text)



(a)



(b)



(c)

Fig.6.3 Power transforms of impulses in Fig.6.2

Fresnel curves, by effectively increasing the amplitudes of irregular data points.

6.3 Measured stellar diameters

Four stellar diameters have been reduced using the classical and scintillation methods. Tb1.6.1 summarises the experimental conditions for the observations. The limb darkening coefficients are taken from Carbon and Gingerich (1969) whenever possible, unless stated. Tbls.6.2 and 6.3 show the results. In addition to the model parameters are given

(i) the RMS error of fit defined as the square root of the average square deviations from the theoretical curve

(ii) the blackbody diameter, calculated from the relation (Allen (1976)

$$\log d_x = \log d_\odot + \log (R/R_\odot) - {}^1/_5 (m-M+5)$$

where d_x is the stellar diameter in m arc sec, $d_\odot$ is the diameter of the Sun in astronomical units and $R/R_\odot$ is the ratio of the star's diameter to that of the Sun.

Figs.6.4 to 6.6 show the classical models fitted to occultations obtained in 1979 under excellent observing conditions. There is only a little scintillation present in each case and the data has a very high signal to noise ratio. Therefore the application of the classical method is valid. For comparison the equivalent point source responses are also plotted against the data, the curves clearly showing increased visibility as compared to the best fit models. The stars are clearly resolved in agreement with diameters larger than the computed limiting resolution. The model diameters are accurate to 5% for star 1, and 9% for stars 2 and 3. The RMS errors of fit are quite small compared to those given by Ridgway et al. (1979).

The scintillation method has been applied to stars 1 and 2. For the former, the computed diameter is increased by 1% and 1.7% for the latter. The RMS errors of fit are reduced and the quoted accuracies are improved by ½% and 4% respectively. Figs.6.8 and 6.9 compare the best fit classical and scintillation models, and for both, the fringes are more closely fitted by the latter.

The fourth occultation has an irregular Fresnel pattern due to a Lunar limb effect, and in comparison to the first three occultations has

Table 6.1

STAR	2 μm	Date d m y	UT h m s	V	K	Sp Type	T	β	Lunar dist.
1	-20474	1.9.79	20.18.0	7.5	2.44	K5	3800	0.35	$3.7\ 10^{10}$
2	-10323	29.8.79	19.59.6	3.9	1.45	G8III	4700	0.25	$3.9\ 10^{10}$
3	-20562	2.9.79	21.55.48	-	2.82	-	5000	0	$3.7\ 10^{10}$
4	-10579	9.1.81	19.58.0		1.86	M4	2900	0.25	$3.7\ 10^{10}$

Occultation parameters

Table 6.2

STAR	Background	Occn. Time m sec	Lunar velocity cm/m sec	Star level	Model diameter m arcsec	Blackbody diameter	RMS error of fit
1	26.91±0.19	89.72±0.17	65.4±0.22	0.924±0.005	5.03±0.25	1	0.019
2	27.94±0.21	81.38±0.22	62.00±.21	0.689±0.004	3.63±0.31	2.7	0.026
3	35.25±0.26	126.92±0.43	30.2 ±.10	1.461±0.008	3.69±0.30	?	0.033
4	9.22±2.11	70.06±0.65	48.78±0.65	6.37 ±0.103	7.25±0.6	3.6	0.041

Results for the classical method

Table 6.3

IRC number	Background level	Occn. time m sec	Lunar velocity cm/msec	Star level	Diameter m arcsec	RMS error of fit
-20474	26.89±0.21	89.81±0.40	65.5±0.35	.925±.011	5.08±0.23	0.017
-10323	28.12±0.19	82.58±0.39	62.8±0.29	.688±.010	3.95±0.18	0.019
-10579	12.64±5.71	78.69±0.89	53.5± .45	6.56±0.4	5.39±0.34	0.029

Results for the polynomial method

much more scintillation. Fig.6.7a shows the best classical model fit. The derived diameter is accurate to 8%. However by eye, one might suspect a better fit from a model with a smaller diameter, but altered in some way, to account for the irregularity of the pattern. For this data, the application of the classical model must be regarded with caution.

The application of the scintillation method reduces the estimated diameter by 25%. There is an improved fit for both the variation in star level and the fringe pattern. The derived diameter is accurate to 6%. Although the RMS error of fit is quite small, the result should be regarded with caution.

Further Developments

Immediate possibilities for the technique are

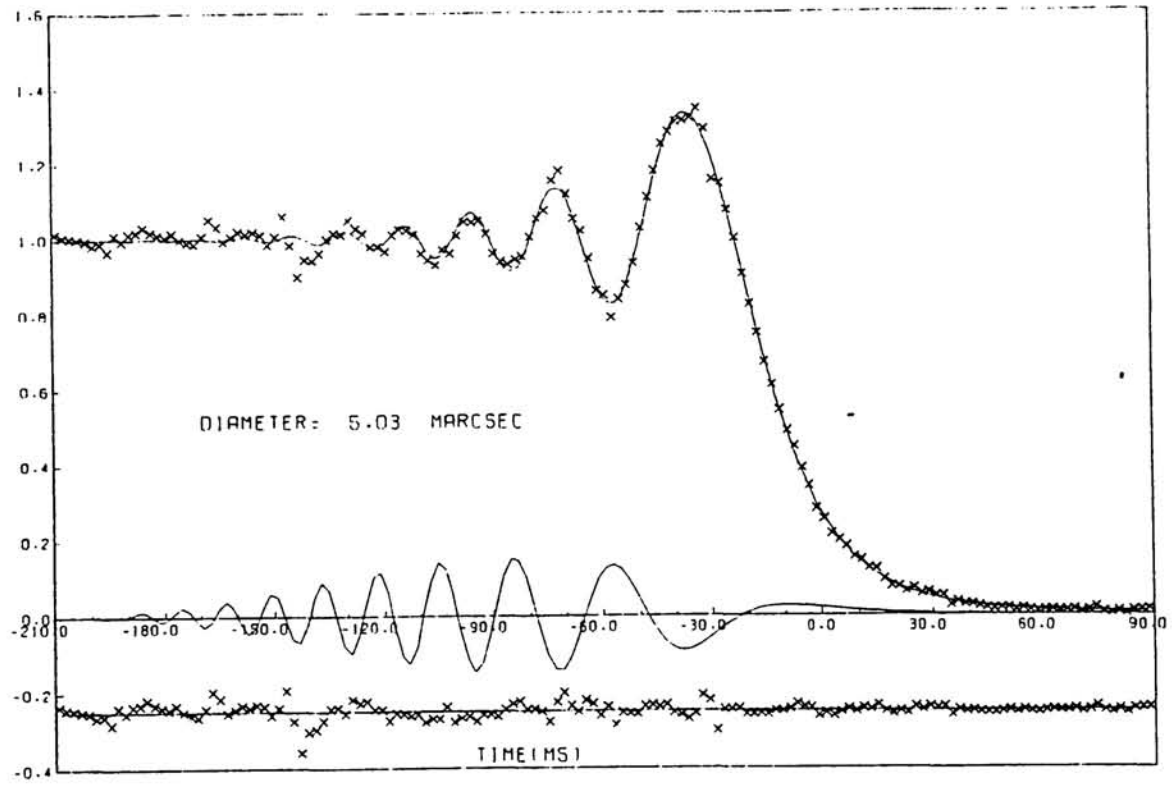
(i) accurate absolute timing of events for stellar positions

(ii) a more accurate bandwidth selection for the data to be modelled (cf. 250 Hz bandwidth is chosen at the moment)

(iii) the forecasting of other objects, e.g. planetary nebulae.

The determination of stellar diameters by the technique at four near infrared wavelengths should be possible later this year. This represents the next major advance for the technique. Possibility exists for the investigation of a differential diameter reduction method.

Until the development of the aperture synthesis the occultation technique will remain the only method for very high angular resolution diameter measurements.



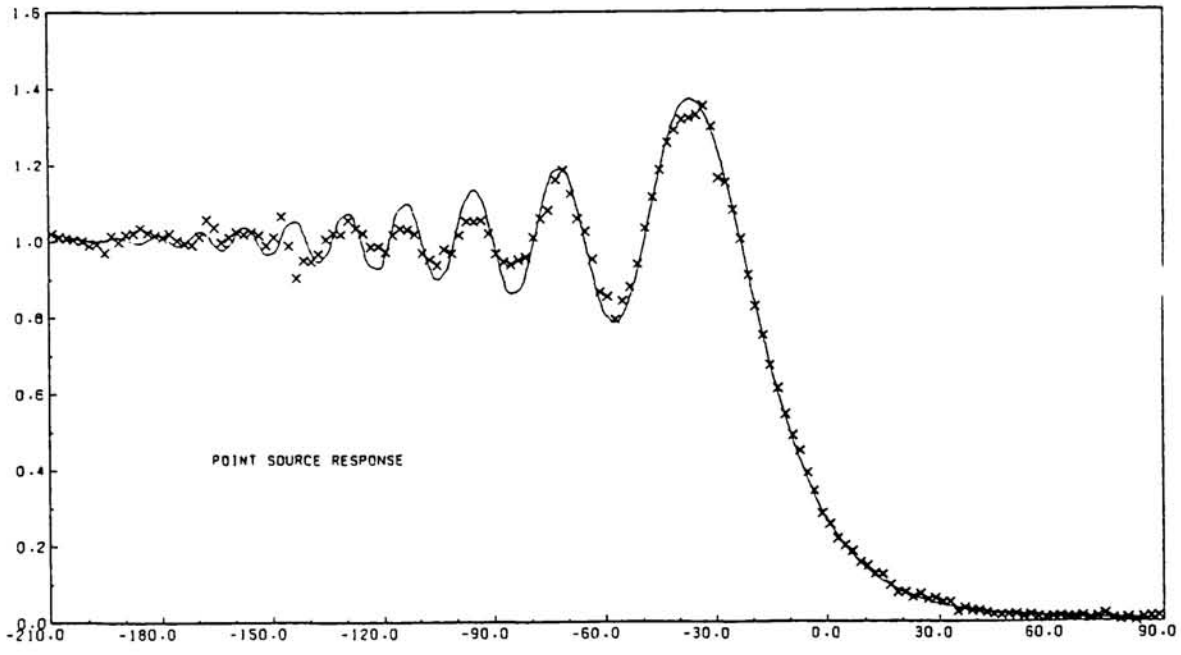
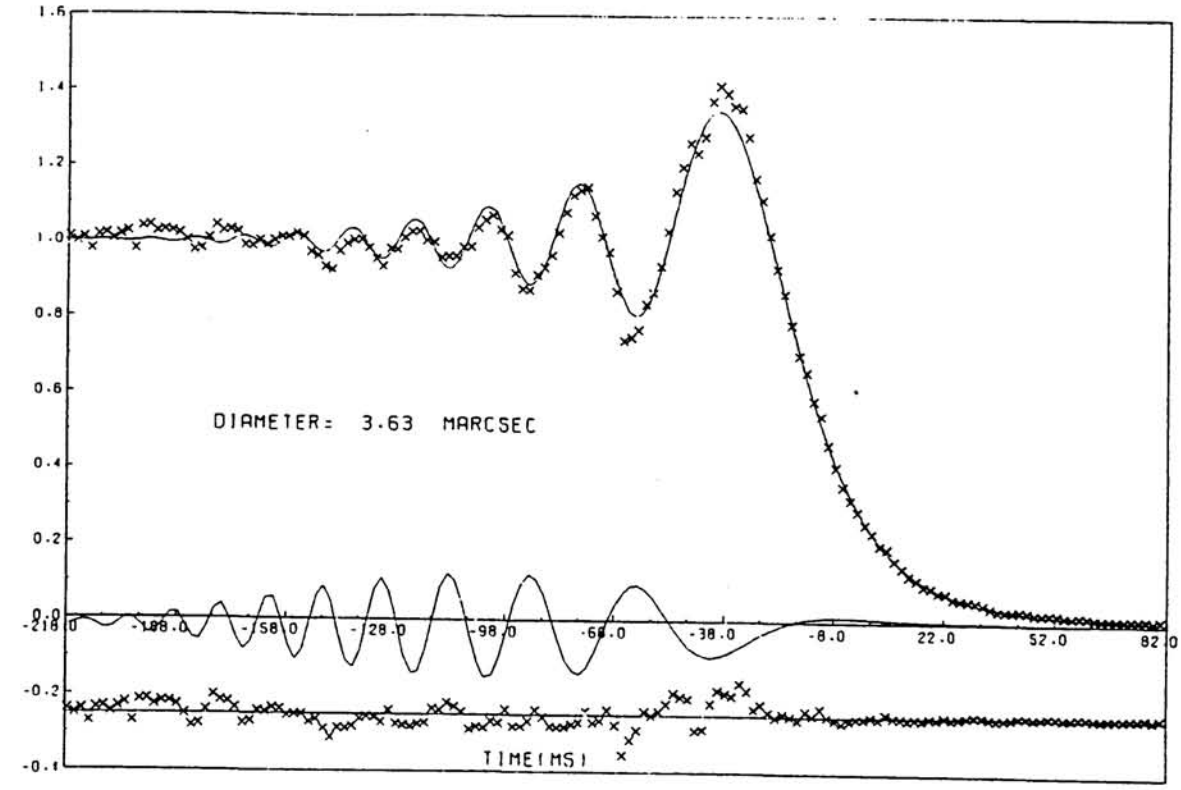


Fig.6.4 Star 1 -20474



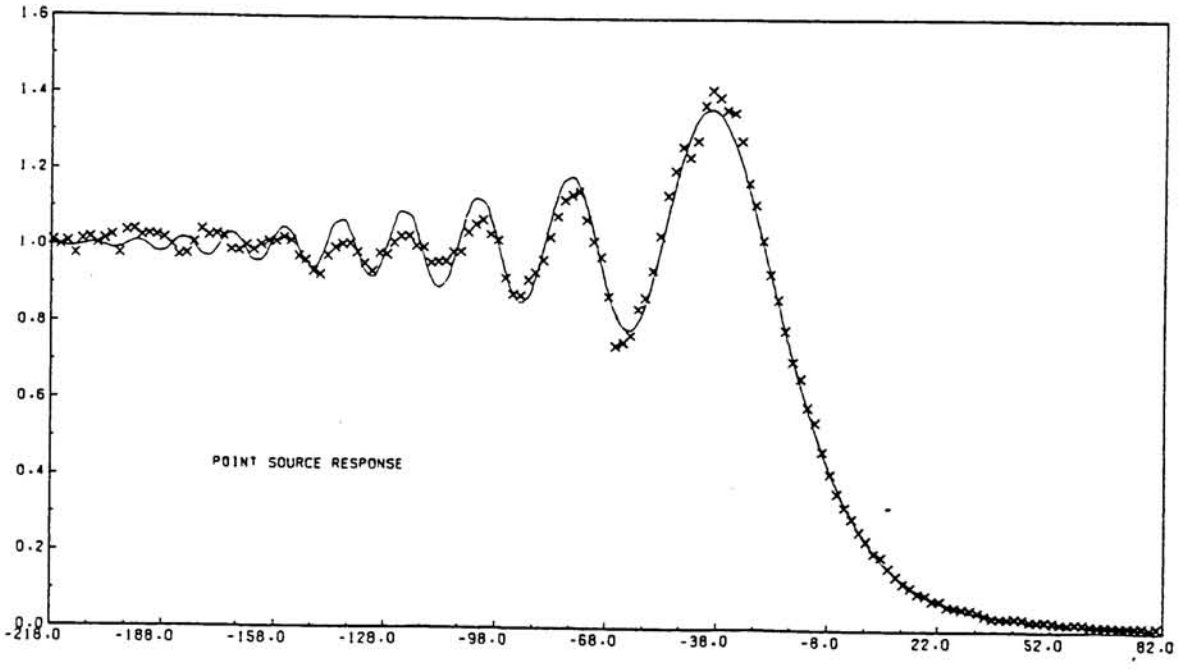
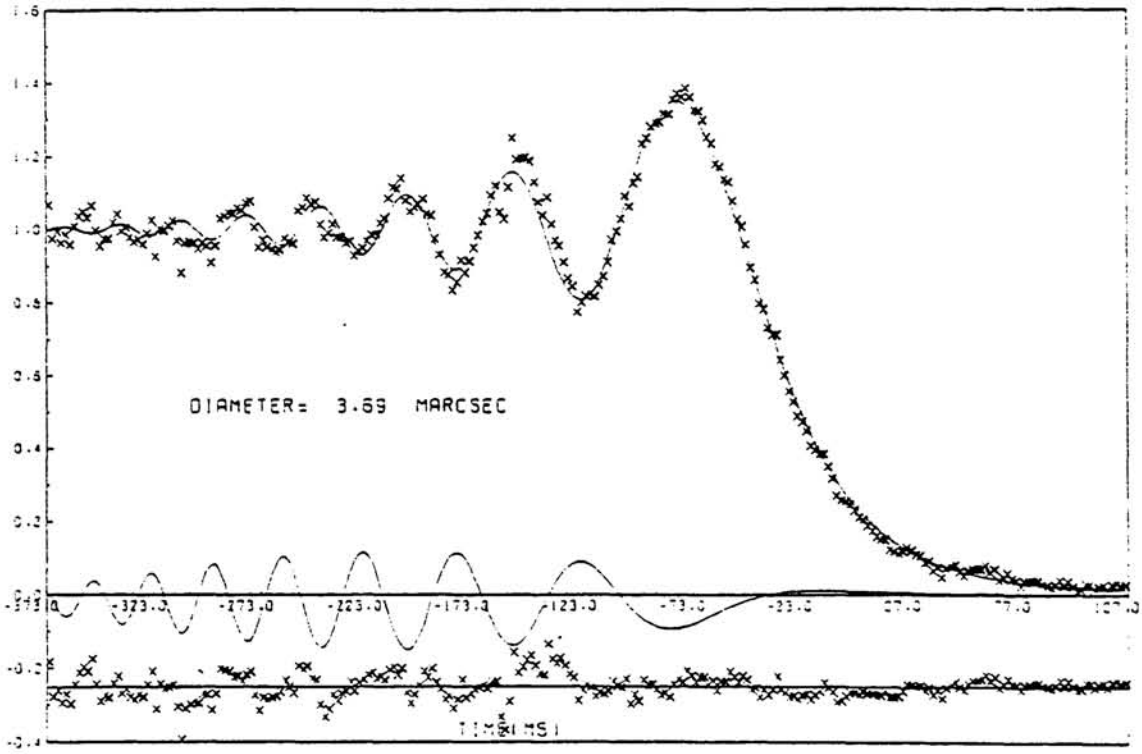


Fig.6.5 Star 2 -10323



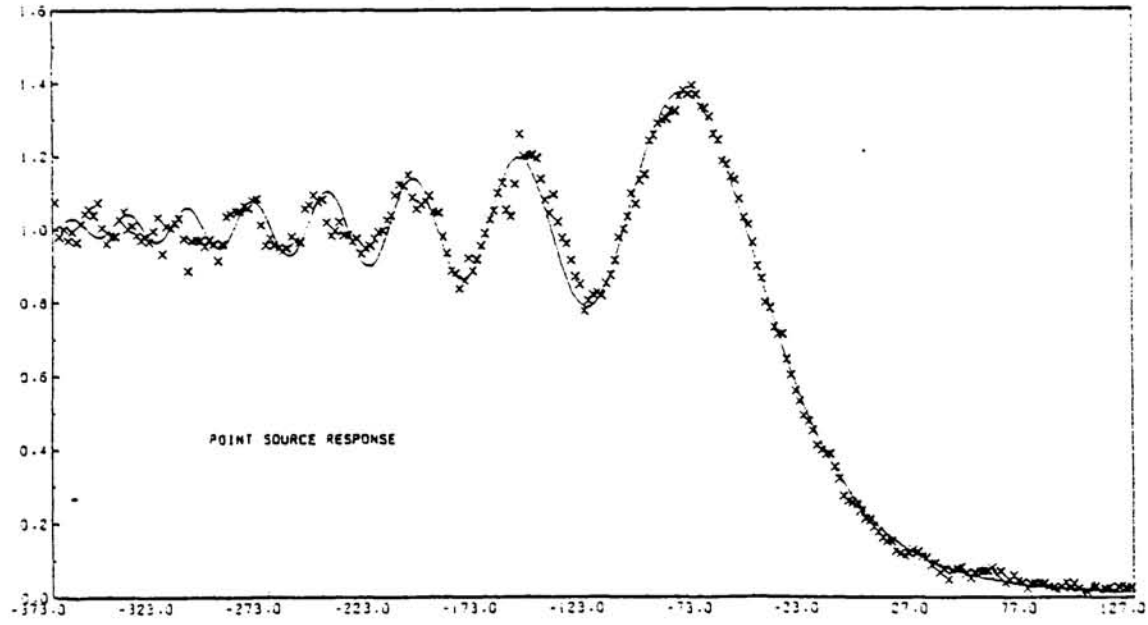
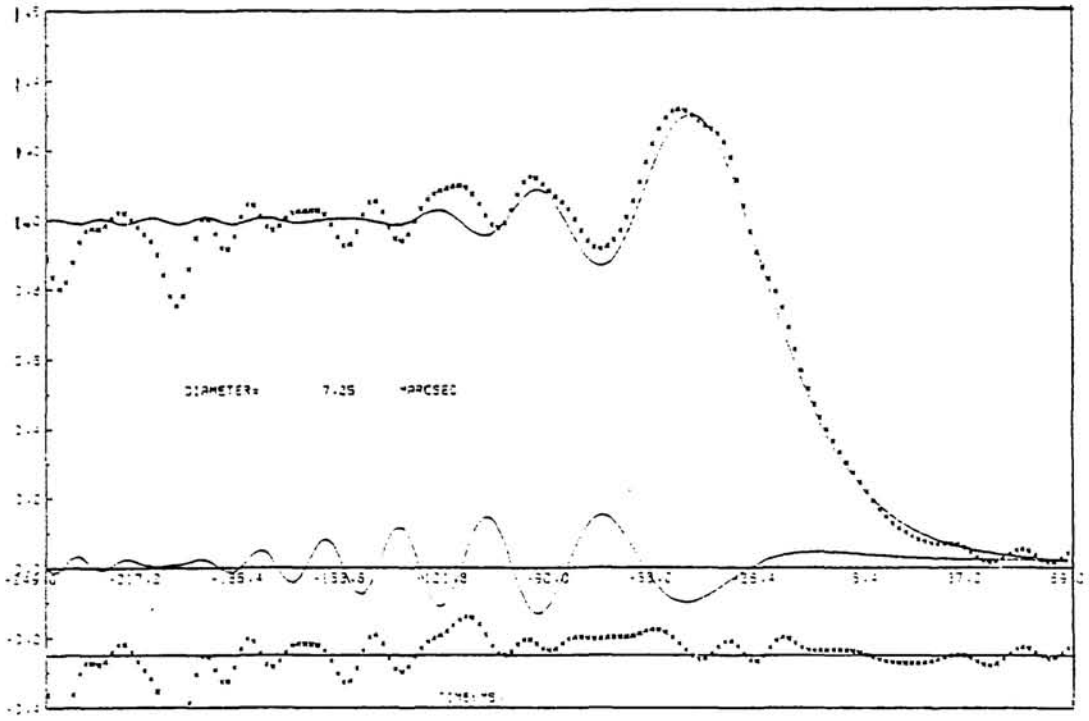
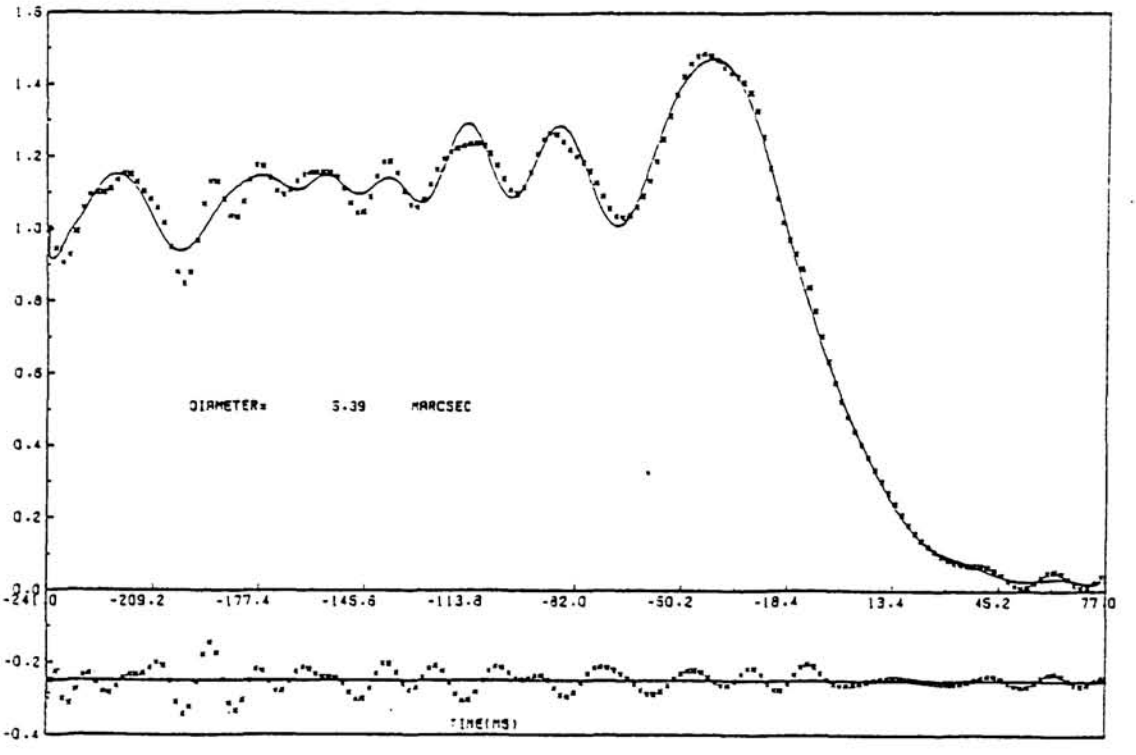


Fig.6.6 Star 3 -20562

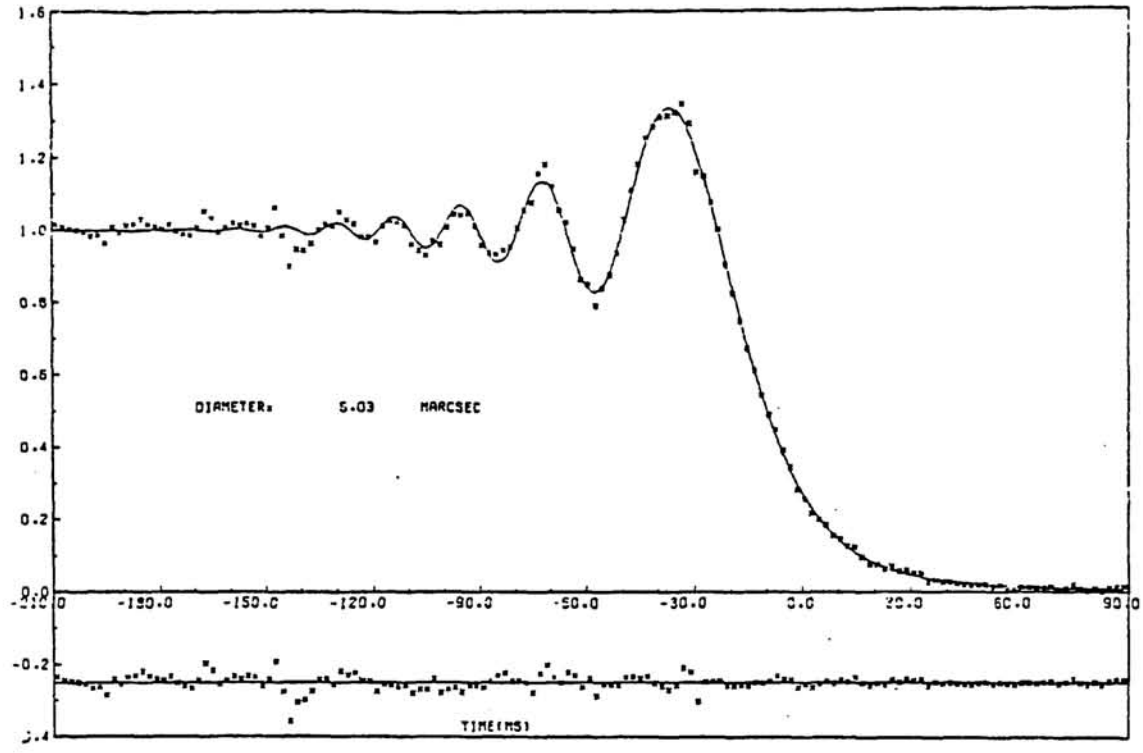


(a)

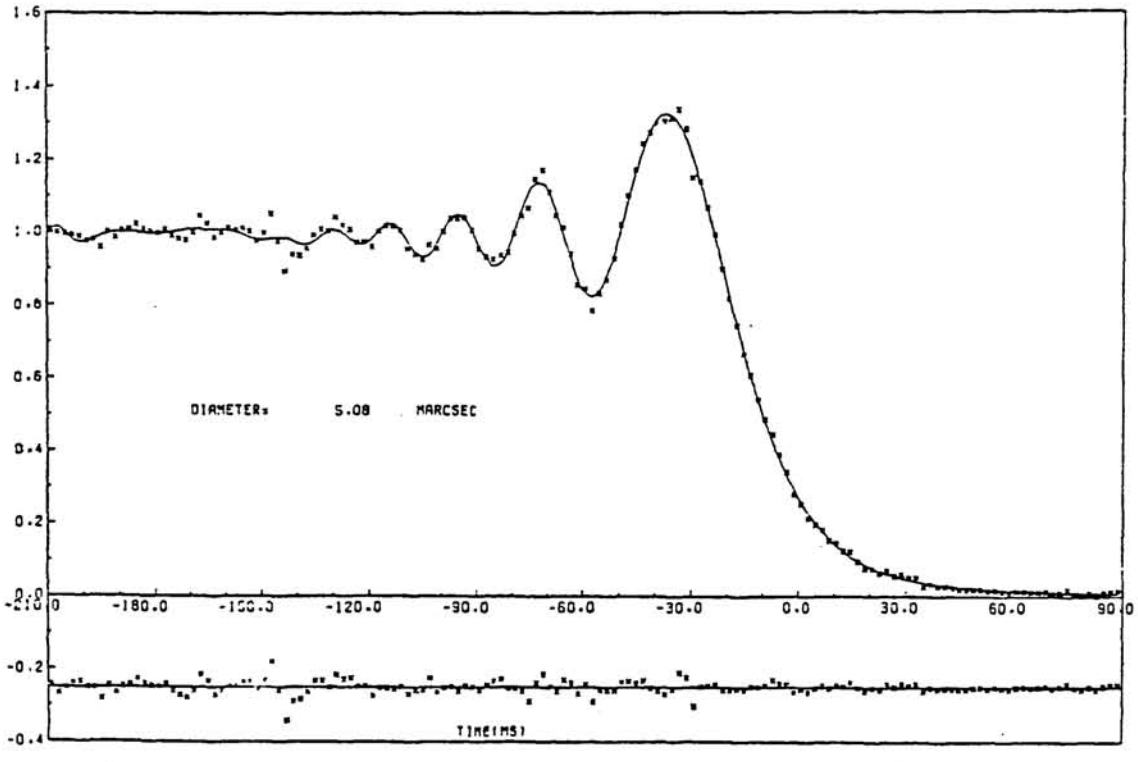


(b)

Fig.6.7 Star 4 (a) classical
(b) including scintillation



(a)

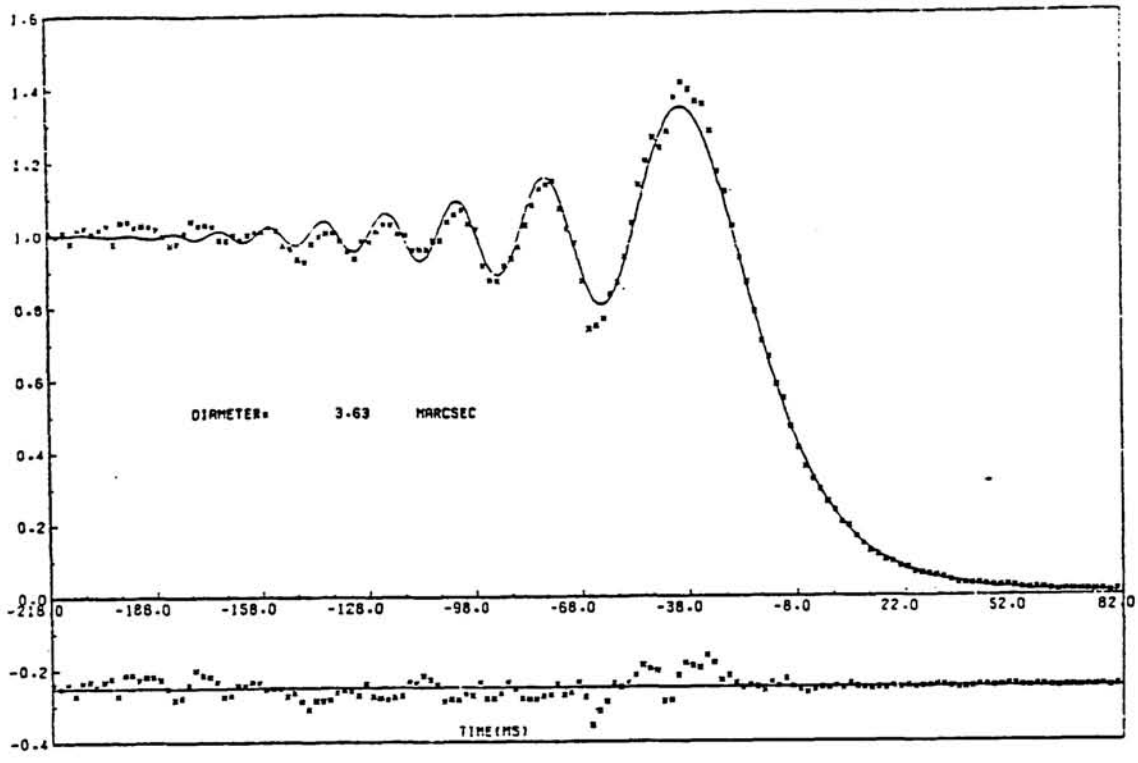


(b)

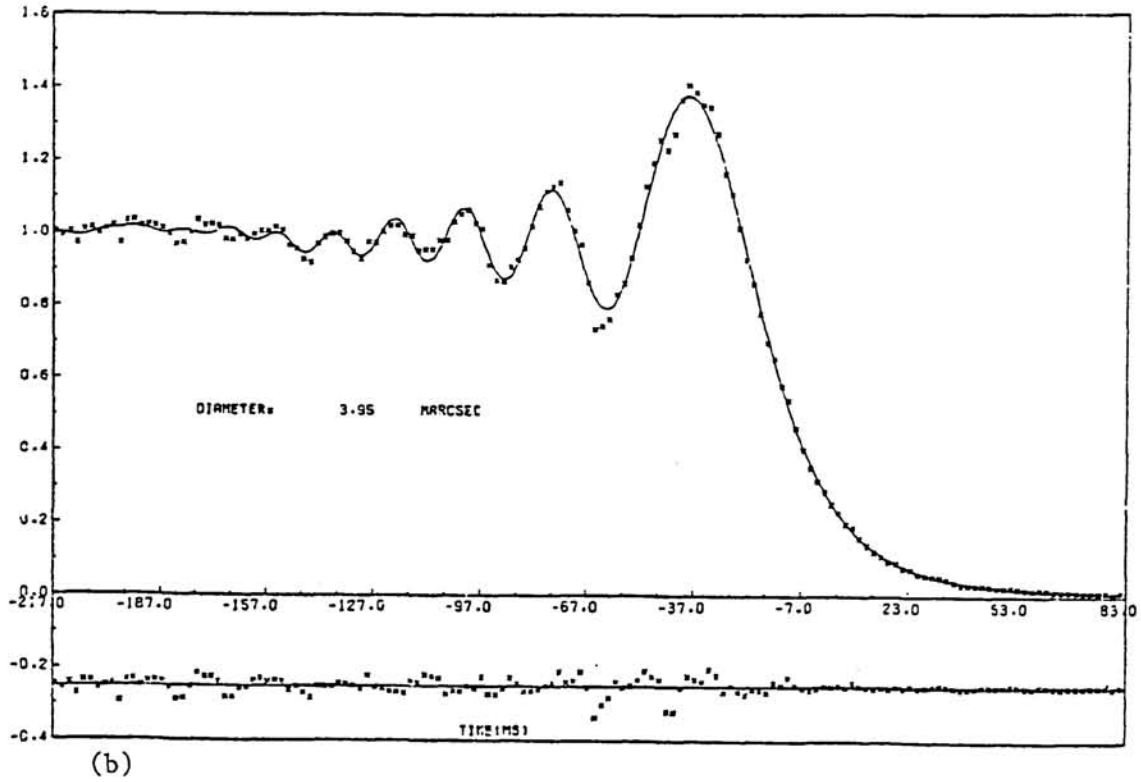
Fig.6.8 IRC-20474

(a) classical

(b) including scintillation



(a)



(b)

Fig.6.9 IRC 10323

(a) the classical method

(b) the polynomial method

Speckle References

Blackwell, D.E. and Shallis, M.J., 1977. Mon.Not.R.astr.Soc. 180, 177.

Burr-Brown. Operational Amplifiers, 1971, McGraw-Hill Book Company.

Foy, R., Chelli, A., Sibille, F. and Lena, P., 1979. Astron.Astrophys. 79, L5.

Fried, D.L., 1966. J.Opt.Soc.Am., 56, 1372.

Hufnagel, R.E. and Stanley, N.R., 1964. JOSA 54, 52.

Knox, K.T. and Thompson, B.J., 1974. Ap.J. Letters 193, L45.

Labeyrie, A., 1970. Astr.Astrophys., 6, 85.

Selby, M.S., Wade, R. and Sanchez Magro, C., 1979. Mon.Not.R.astr.Soc., 187, 553.

Sibille, F., Chelli, A. and Lena, P., 1979. Astron.Astrophys. 79, 315.

Talarski, V.I., 1961. Wave Propagation in a Turbulent Medium, McGraw-Hill Book Company.

Occultation References

Allen, C.W. Astrophysical Quantities, 1976.

Born, M. and Wolf, E., 1975. Principles of Optics, Pergamon (5th Edition revised).

Carbon, D. and Gingerich, O.,1969. Theory and Observation of Normal Stellar Atmospheres.

Diercks, H. and Hunger, K., 1952. Z.Astron., 31, 182.

Knoechel, G. and Heide, K. Von der., 1978. Astron.Astrophys., 67, 209.

MacMahon, P.A., 1909. Mon.Not.R.astr.Soc., 69, 126.

Nather, R.E. and Evans, D.S., 1970. Astron.J., 75, 575.

Nather, R.E. and McCants, M.M., 1970. Astron.J., 75, 963.

Ridgway, S.T., Wells, D.C. and Joyce, R.R., 1977a. Astron.J., 82, 414.

Ridgway, S.T., 1977b. Astron.J., 82, 511.

Ridgway, S.T., Wells, D.C., Joyce, R.R. and Allen, R.G., 1979. Astron.J., 84, 247.

Whitford, A.E. 1939. Astrophys.J., 89, 472.